ABSTRACT

DUEMMLER, KAI ERIC. Bubble Nucleation and Growth in Alloy HT9 through the use of In-Situ TEM: Sequential He-Implantation and Heavy-Ion Irradiation versus Dual-Beam Irradiation (Under the direction of Dr. Djamel Kaoumi).

HT9 is a Ferritic/Martensitic alloy envisioned as a candidate for structural and cladding applications in the next generation of nuclear reactors such as the SFR. In this study, the formation of He bubbles is investigated through the use of in-situ Transmission Electron Microscopy coupled with He implantation and Heavy ion irradiation. Of particular interest is the effect of increasing the He appm/dpa ratio on the formation and growth of the bubbles, as well as the effect of the sequential order of irradiation i.e. He-pre-implantation followed by Heavy ion irradiation versus true dual-beam irradiation.

Bubble Nucleation and Growth in Alloy HT9 through the use of In-Situ TEM: Sequential He-Implantation and Heavy-Ion Irradiation versus Dual-Beam Irradiation

by
Kai Eric Duemmler

A thesis submitted to the Graduate Faculty of
North Carolina State University
in partial fulfillment of the
requirements for the degree of
Masters of Science

Nuclear Engineering

Raleigh, North Carolina

2020

APPROVED BY:

_____	_____
Dr. Djamel Kaoumi Chair of Advisory Committee	Dr. Mohamed Bourham
_____	
Dr. Benjamin Beeler	

DEDICATION

I dedicate this thesis to my lovely wife Ashley who put up with me through this whole process and my family for their love and support.

BIOGRAPHY

I completed my Associates of Science from South Piedmont Community College in 2016. Following this I received my Bachelor of Science in Nuclear Engineering from North Carolina State University.

ACKNOWLEDGMENTS

I would like to acknowledge Dr. Ce Zheng and Dr. Djamel Kaoumi for conducting the experiment, and for Dr. Zheng's work in the sample preparation and Dr. Cedric Baumier and Dr. Aurelie Gentils for their technical support during the experiment, at the JANNuS-Orsay facility. This work was performed in part at the Analytical Instrumentation Facility (AIF) at North Carolina State University, which is supported by the State of North Carolina and the National Science Foundation (award number ECCS-1542015). The AIF is a member of the North Carolina Research Triangle Nanotechnology Network (RTNN), a site in the National Nanotechnology Coordinated Infrastructure (NNCI).

TABLE OF CONTENTS

LIST OF TABLES

LIST OF FIGURES

Chapter 1:

INTRODUCTION

1.1 Motivation for the Study

1.1.1 The motivation for studying alloy HT9

The motivation behind studying HT9 is that it is a potential cladding material for several next-generation nuclear reactors (generation IV reactors). The limitation of next-generation reactors is often material limitations and working on steel that could be used in several different designs benefits the entire industry. HT9 is a good candidate for the next generation reactors due to its resistance to swelling [5-7]. With many of the next-generation reactor designs the dose that the structural and cladding materials will face in the lifetime is expected to be much larger than that or the current light water reactors domination the current nuclear fleet going to 100 plus dpa depending on the design. With higher dose comes more swelling of the irradiated materials and this is why swelling resistant materials are being considered for core components.

1.1.2 The motivation for studying helium

In nuclear reactors, the cladding material is exposed to fast neutron flux for fast spectrum reactors and fast and thermal spectrum neutrons for thermal reactors. HT9 is a cladding material suggested for fast reactors. One common reaction that occurs in the nuclear reactor is the (n, α) reaction in which a neutron interacts with the material in the core, could be fuel, clad, or structural and causes a helium atom to be produced through alpha decay. This helium atom can now interact with the vacancies that are presented due to thermal equilibrium and/or produced by radiation damage or migrate through the matrix and interact with other sinks or even escape the metal if it is near a free surface. If trapped in the metal, it can stabilize cavities and lead to bubble formation and eventually swelling.

1.1.3 The motivation for studying the effect of helium appm/dpa ratio

The motivation for studying the rate of helium implantation per dpa is to understand how helium will change the microstructure. In a nuclear reactor, the rate of helium implantation in the material is constant since nuclear power plants tend to stay at full power during their operational cycle, which means that the flux of neutrons stays constant in each area of the core. The flux will vary both axially and radially, but for the same location it stays constant, there are fluctuations especially near the end of life when the power plants are running at lower power. Since ions induce damage faster than neutrons, it is important to study the influence of the rate of helium implantation. When trying to emulate neutron irradiation with ions we need to find the right dpa/s and He/dpa values to induce corresponding microstructure development under neutron irradiation in the reactor. Not only will this allow for easier “simulation” of neutron damage by ions plus helium but also an understanding of helium in the mechanics of bubble formation and growth. The other advantage is to understand better the effect of different implantation rates that could be seen in the cladding due to fuel shuffling into various parts of the core during each reloading phase and the axial/radial position within the core.

1.2 Motivation for using ion irradiation

In many irradiation experiments, using neutron irradiation would be too costly, time consuming and potentially dangerous due to activation of the samples. Not only does it take longer to reach higher doses but the sample will have to be either handed in hot cells or to be stored until the activity reaches a safe level to be handled. This is why ion irradiation is a popular method to create irradiation damage in research. Ions can emulate the displacement cascade damage that neutrons can induce but it does not reproduce the nuclear reactions that neutrons do, so it does not activate the samples. This is a distinct advantage since it allows for safe handling

of the samples, however, this also is a source of error when using ion irradiation to simulate neutron irradiation. As mentioned earlier the (n, α) reaction is one of the main nuclear reactions so to simulate the production of helium within a material, the sample can also be implanted with helium while irradiated with a heavier ion to induce displacement damage, hence the interest in dual-beam irradiations.

Although, simultaneous dual-beam irradiation would emulate the formation of helium particles while displacements are generated at the same time, there is also the possibility of doing sequential irradiations, i.e. implantation then irradiation or irradiation then implantation. This also brings up the question if this order matters at all with the selected materials. In terms of influence the bubble size, distribution, and influence on the swelling of the material in question, here HT9 steel. Jublot-Leclerc et al. [8, 9] have suggested that in the case of stainless steel 316 L (SS 316 L) it does matter.

1.2.1 Goal of this study

There are two main goals of this study. The first goal is to understand the influence of He atomic parts per million (appm)/ displacements per atom (dpa) on the swelling behavior of the material. The rate of helium implantation could influence the swelling and bubble size distribution. Helium is used to emulate the helium produced in the nuclear reactor from the (n, α) reaction. The other goal of the study is to determine sequential irradiation versus dual-beam differs. This portion will analyze the results for sequential implantation of helium then gold ion irradiation compared to dual-beam irradiation. The results of this study can influence the future of ion irradiation since how helium is accounted for will be an important factor.

1.3 Background on radiation damage

Radiation damage i.e. the formation of point defects by irradiation can be done with ions, electrons, or neutrons. The unit that is associated with damage is displacements per atom or dpa. X dpa means that on average each atom has been displaced X times. This unit is used to compare damage between different experiments. This study focuses on ion irradiation specifically gold and helium ions.

Some general differences between neutron, electron and ion irradiation is that neutron is isotropic radiation, while the other two are directional, based on the location of the source is. The displacement rate (dpa/s) also varies with neutrons being the slowest and electrons being the fastest, the time of irradiation follows the same trend with neutrons irradiation lasting months to years; ions irradiation on the scale of hours while electrons irradiation tend to be on the order of minutes. The temperature of the experiments also varies, with ions and electrons it depends on the setup but neutrons they are conducted in nuclear reactors and are limited to the temperature profile within the core. Another major difference is the amount of sample that is influenced. In the case of neutron irradiation, the bulk sample will be irradiated while ions have a penetration depth profile that is often calculated with SRIM [10] but it limits the damage to the surface. This causes neutron irritation to be homogeneous while ion irradiation is inhomogeneous.

The way particles cause damage is that when an energized particle comes and interacts with the atoms three things can happen. If they are a charged particle such as ions or electrons, they will lose energy due to interaction with the electrons and the amount varies based on the initial charge, energy and the mass of the charged particle. The other two things that can happen are the interaction with the nucleus of the target, it can either undergo a nuclear reaction, which is more common for neutrons then ion or it can undergo an elastic collision. In this study the

particles used are ions (gold and helium), they do not cause nuclear reactions so the only two terms that remove energy are the electron and the elastic collisions. The target in this study will primarily be iron but also includes the alloying elements as well, which can be seen in the composition of HT9. When calculating the energy transferred, it is assumed a binary elastic collision where the nucleus is a stationary target. The transferred energy can be seen below in equation 1.2.1, where T is the transferred energy, E is the energy left after interacting with the electrons θ is the scattering angle of collision in the center of mass system and Λ is a mass ratio seen in equation 1.2.2. M_1 and M_2 are the masses of the incoming particle and the collided particle, respectively. In this study that would be for gold and iron respectively.

$$T = \frac{1}{2}\Lambda E(1 - \cos(\theta)) \tag{1.2.1}$$

$$\Lambda = \frac{4M_1M_2}{(M_1 + M_2)^2} \tag{1.2.2}$$

In a head-on collision θ would be equal to π allowing for the maximum energy transfer to be ΛE and the minimum energy that can be transferred is when θ is zero then the energy it can transfer is also zero. The energy lost due to interactions with electrons can be seen in equation 1.2.3 where I is the ionization potential and E^* is the energy remaining that can go the energy transfer equation in place of E.

$$E^* = \frac{I}{\Lambda_{\mathrm{PKA-e^-}}} \tag{1.2.3}$$

The Λ_{e^-} in equation 1.2.3 has different masses then the Λ in equation 1.2.2 and they would be the mass of an election and that of the incident particle (gold ions).

When the energy transferred is above a displacement threshold, the atoms can be displaced. The atoms that are displaced by the incident particles are called primary knock-on atoms or PKA. If the energy transferred to the PKA atoms is large enough they can collide with other atoms and displace them created secondary knock-on atoms and so on. When one PKA is of such large energy it can cause a sequence of collisions to occur which displace the next atom this is called a cascade. This is something that usually occurs during ion or neutron irradiation. Electron irradiation causes point defects but they do not have sufficient mass to create a cascade. Neutrons and ions are heavier so the energy transfer per collision will be larger, particularly for ions were Λ could be one if the matrix and ions are the same material. In a nuclear reactor, cascades happen due to the energy of the fission neutrons, which are around 1 MeV; this allows cascades to be formed. A cascade is an area with a large number of point defects that can interact with each other. Since each displaced atom leaves a vacancy behind and becomes an interstitial atom. Interstitial atoms can migrate easier the vacancies since their energy of migration is lower. In the case of ions due to the larger mass, they do not need to be as energetic as neutrons to produce the same cascades since they will be able to transfer more of the energy in a single collision.

The sequence of events leads up to cascade and following it are described here. To form a cascade, one energetic particle causes a sequence of collisions within the material in a localized area. In a cascade the energy transfer happens very quickly during each consecutive collision, once the energy is below the threshold of displacement it will still transfer energy but it will no longer displace the atom. This transferred energy is released in the form of phonons this creates a thermal spike at the point of peak damage. This thermal spike allows some of the damage to heal itself as it cools down to the bulk temperature. This healing is the interaction between vacancies

and intestinal atoms and results in the annihilation of the point defects. While it is cooling the intestinal atoms move away from the cascade area, faster than the vacancies, this creates a depleted zone with a larger concentration of vacancies. During this time there is a thermal migration of defects that can interact with the sinks in the material. These sinks could be grain boundaries, precipitates or other point defects. One common way that the displacement damage is calculated is with the NTR method [11] which is a modified Kinchin Pease method [12].

E_d is the displacement threshold and for metals it is around 40 eV [13, 14] and 28 eV for nonmetals [10]. A Frenkel-pair is a point defect that can form due to irradiation. It is defined as an interstitial atom and a corresponding vacancy, which can be the result of elastic collision [15]. These Frenkel-pairs can recombine which is why the peak damage and the final damage difference since vacancies and interstitials from different Frenkel-pairs, recombine and annihilate each other. The interstitials or vacancies can meet other point defects of the same kind and agglomerate to form precipitates or cavities respectively.

1.4 Literature Review on HT9 Steel

1.4.1 Background on HT9

HT9 is a 12Cr-1Mo-0.5W ferritic/martensitic steel developed as a core material in the Gen IV reactors and for the first wall of fusion reactors [16]. It was designed to replace AISI 316 due to strong swelling resistance [17-19] in fast breeder reactors that operated at high temperatures were corrosion resistance of AISI 316 was not needed. It has also been shown that HT9 can maintain properties at doses as high as 175 to 200 dpa [16]. This is desired as the Gen IV reactor designs are pushing the upper dose limit up.

1.4.2 Neutron Irradiated HT9

1.4.2.1 Swelling and Bubble Size Distribution

HT9 was irradiated in BOR 60 reactor and showed cavity formation with observed average sizes of 1.1 -1.5 nm when observing cavities smaller than 2 nm for temperatures 650-730K and dose range of 14.6-18.6 dpa [19]. Cavities are the agglomeration of vacancies within a material. When looking at cavities larger than 2 nm, they were only observed in the case of 690K where the size was 5.4 nm [19]. These cavities are created by neutron irradiation, as HT9 does not have cavities in the as-received state. In a different study Zheng et al. [1] looking at the effect of dose. The results of their study can be seen in figure 1.3.2.2.1, what can be seen is that as the dose increases the distribution changes form a unimodal to a bimodal distribution.

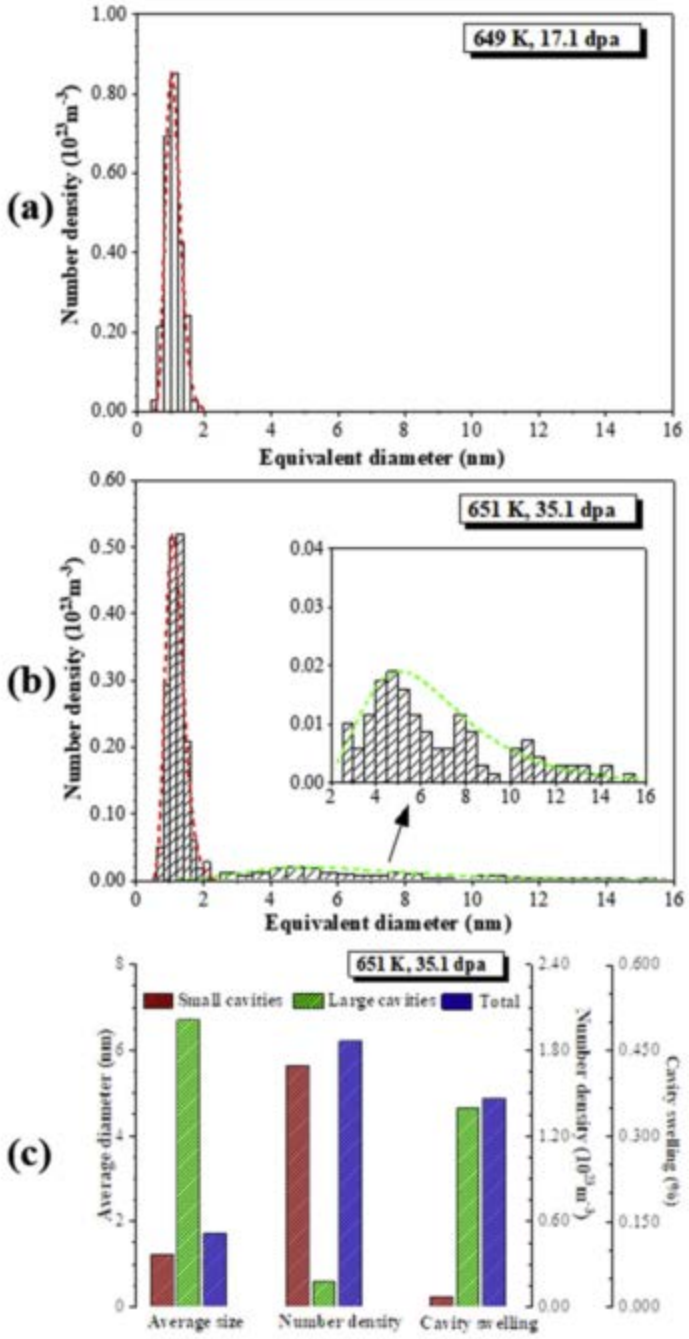

2

Figure 1.4.2.1.1: Effect of dose on the size distribution, average size, number density for 17.1 dpa and 35.1 dpa at 650 K for HT9 [3].

On observation here is that the size of the small cavities does not increase much but it does transform into a bimodal distribution with a few larger bubbles.

The swelling of HT9 is also influenced by dose, this can be seen in [1, 19]. For the case of dose the swelling increases from 0.02% to 0.37% for a dose increase from 17.1 to 35.1 dpa [1]. The Temperature has a lesser effect of swelling then dose does but can be seen in Zheng et al. [19] that the swelling varies from 0.02 to 0.09%.

1.4.2.2 Second Phases

The microstructure of HT9 is altered when it is exposed to neutron radiation. When HT9 is irradiated with neutrons Zheng et al. [19] observed two different precipitates, Mn/Ni/Si-rich and Cr-rich precipitates called G-phase and α' prospectively. The exact stoichiometry of G-phase is $Mn_6Ni_{16}Si_7$ [20]. The sizes of these precipitate are smaller than the $M_{23}C_6$ carbides and vanadium nitride that can be found in as received HT9 with an average size of 6.1 to 19.8 nm for G-phase and 6.5-10.4 nm for α' [19]. Both G-phase and α' precipitate at lath boundaries, but G-phase was also observed on dislocations within the grains [19]. As the temperature increases the density of the precipitates decreases and this is a drastic reduction, by 3 orders of magnitude in case of G-phase [19]. According to simulation G-phase does not form without irradiation above 643 K [19]. This could explain the drastic reduction as the size went from 650 to 730 K. Second phase precipitates are formed by cascades that cause an enhanced diffusion of solute atoms [19]. A similar case is observed for α' where its formation is caused by radiation-enhanced diffusion and is dependent on dose and temperature [19]. Another observable radiation-induced segregation (RIS) is the phenomenon where Ni and Si segregate to cavity surfaces. Zheng et al. [1] state that is behavior occurred regardless of the cavity size. The segregation to bubble cavities could impact the behavior of swelling.

1.4.3 Ion Irradiated HT9

Ion irradiation is common due to allowing irradiation studies to take place much faster without activating the material. To simulate the production of helium in HT9 one can implant helium at the same time as the heavy ion irradiation or energetic e^- causing the displacements or doing it before/after the heavy ion irradiation.

1.4.3.1 Dual-Beam Irradiation

There have been dual-beam studies of HT9 conducted in the 1980s. Some of these studies looked at the effect of irradiation temperature on dual-beam irradiation [21] while others looked at a single heavy ion beam versus dual-beam at various temperatures [22].

In the study by Suzuki et al, [21], they irradiated HT9 and HT9 modified +2 wt.% Ni, with 3.0 MeV Ni^+ ions and degraded 0.83 MeV He^+ ions in a temperature range from 410-600 °C. The implantation rate per dpa was 15 appm He per dpa and the total damage was 25 dpa. They observed that swelling in HT9 was highly accelerated at 750 K compared to other temperatures and that the addition of nickel also swells but the swelling was suppressed when compared to the HT9 without nickel case. The dual-beam + electron irradiation resulted in a bimodal distribution in size where the smaller size does not appear to be temperature depended or dpa dependent while the larger bubbles do [21].

The other study conducted by Asano et al. [22] dual-beam study was carried out at 5 and 15 appm He per dpa with a temperature range from 410 to 600 °C with the same ions and energies as the last study. The larger doses with high temperatures produced a bimodal size distribution. In their study it can be observed that at the same dpa level the size of the bubbles is temperature dependent with maximum size at 743 K [22]. At 623 K the size of the bubble was around the resolution limit of their equipment at 2 nm and for the 863 K case the bubble size was less than 4

nm but a uniform size [22]. Besides dual-beam studies conducted on HT9, there have also been sequential studies where helium is implanted then irradiated with heavy ions or irradiated with heavy ions then implanted with helium.

1.4.3.2 Sequential Implantation of Helium then Irradiation

There have been studies done on HT9 that focus on the swelling, where the HT9 was pre-implanted by helium to a certain amount and then irradiated with some charged particle. One such study was conducted by Kai and Kulcinski [23] where they pre-implanted helium 100 appm He into HT9 and then irradiated it with 14 MeV Ni^{2+} ions. The irradiation temperatures were 300 °C to 600 °C with increments of 100 °C and the dose rate was $1*10^{-3}$ dpa/s with a max dpa of 200 dpa. What they observed was that voids only formed in the case of 500 °C with a dose of 30 and 60 dpa [23]. Smaller helium bubbles were observed at 500 °C with 30 dpa and for 600 °C at both 10 and 30 dpa [23]. Other observations by Kai and Kulcinski[23] is that pre-implantation enhances the growth of voids at higher temperatures of 500 and 600 °C. They also showed that overall all swelling was low less than 0.1%. The last important finding was that there were no microstructural differences at 600 °C between the irradiated samples and the non-irradiated samples indicating the dominant nature of thermal diffusion [23]. This shows the upper-level limit of the temperature range that HT9 should be used in.

In a different study by Getto et al. [24] they determined that pre-implanted helium leads to void swelling by shortening the nucleation regime when the dose was low but at transient regime, the growth was hindered by the helium. In their study [24], they pre-implanted the HT9 with 0, 10 or 100 appm He and then using 5 MeV Fe^{2+} ions created dose up to 375 dpa with a temperature range from 400 to 480 °C. What they observed is that the void growth rate was

independent of temperature for 93 to 375 dpa and they suggest that there is a temperature-independent steady-state swelling rate [24].

In a different study by Getto et al. [25] where the conditions were the same as the last study except the dose was 140 dpa and at 440 °C where the difference was how the irradiation was conducted. The two modes they tested was raster-scanning the beam over the sample or to defocus the beam and irradiate the whole sample at the same time. For the raster-scanning what was observed was that the bubble size decreases with an increasing amount of appm helium while the density and swelling increased with increasing appm He [25]. For the defocused case there is no linear trend for bubble size but bubble density increases with appm He. Their study concludes is that there are measurable differences between the different irradiation modes, in defocused mode, precipitates, voids and dislocation loop diameters were larger than the raster-scanning counterpart [25].

1.4.4 Differences Between neutron and ion irradiation

There are some differences created between neutron and ion irradiation besides the helium production. On such example is α' which rarely forms when irradiated with ions but is observed when irradiated with neutrons [1, 26]. According to Pareige et al. [26] a reason this occurs is the time is too fast since ion irradiation is on terms of hours not months to years like neutrons and the dose is too large. Other precipitates that do not form under ion irradiation besides Cr-rich α' are χ, and η (M_6X) phase which is also seen in neutron irradiation [4].

Other differences are the rate of helium generation and the fact that nuclear reaction can produce other elements not normally found in the metal matrix during neutron irradiation. This cannot occur during ion irradiation, as the interactions are primarily elastic collisions and not nuclear reactions.

CHAPTER 2:

EXPERIMENTS AND METHODS

In this chapter, the materials and the experimental procedure for this study are described. This includes the materials used, sample preparation, initial characterization, and the procedure of the experiment and the analytical methods. Dr. Kaoumi and Dr. Zheng conducted the experiments.

2.1 Materials

The material used in this study was Ferritic/Martensitic steel HT9. The chemical composition for this steel is given in table 2.1.1. The samples were received from Los Alamos National Laboratory (LANL).

Table 2.1.1: As received HT9 nominal and measured composition (wt.%) [1].

	Fe	Cr	Mo	Ni	Mn	W	V	Si	C	P	N	S	Cu	Al
Nominal	Bal.	11.8	1.03	0.51	0.5	0.5	0.33	0.21	0.21	0.008	0.01	0.003	-	-
Measured	Bal.	12.3	10.7	0.61	0.49	0.49	0.28	0.24	0.198	0.012	0.005	0.001	0.063	0.022

The heat used in this study was 84425, which means the HT9 has a tempered martensitic structure. The heat treatment that was used was normalization at 1038 ºC for 5 minutes followed by air-cooling. This is followed by tempering at 760 ºC for 30 minutes again followed by air-cooling. The measurements revealed the presents of copper and aluminum within the HT9, which is not part of the nominal composition.

2.2 Sample Preparation and Material Characterization

2.2.1 Sample Preparation

The sample preparation was to polish the surface of the material using a Pace Technologies NANO 1000T GRINDER-POLISHER© with silicon carbide (SiC) grit paper to a

finish of 800 grit. Following this the transmission electron microscope (TEM) samples were prepared using the FEI Quanta 3D FEG a focused ion beam (FIB) and a scanning electron microscope (SEM) dual-beam instrument at the Analytical Instrument Facility (AIF) at North Carolina State University. The TEM sample preparation can be broken into 3 steps, the first is the hog-out of the sample then mounting it to the TEM sample grid followed by the final thinning step. In the first step the first thing that needs to be done is to place a platinum layer down to protect the sample's surface, this is normally 2-3 µm thick, 2 µm wide and as long as the sample needs to be in this case 20 µm. The next step is the hog-out step. In this step, the space to the sides of the platinum is removed. The dimensions for the hog-out steps are 30 µm by 25µm for the top and 30 µm by 15 µm for the bottom and the target depth was 10 µm. The first step in removing the sample to mount it is the inverted J-cut and in this step, an inverted J is cut below the sample. This means only a small portion is holding the sample. Then the needle is inserted and platinum is used to attach to the needle and then the last portion is removed. Then the sample is attached to the mount with platinum again. In the final thinning step, more material is continually removed until the sample reaches electron transparency and then the final polishing step is used to remove fib damage.

The Author would like the thank, Dr. Zheng, as he handled the sample preparation.

2.2.2 As Received HT9

The initial microstructure of HT9 has martensitic lath, in packets within prior austenite grain boundaries (PAGBs). Preexisting carbides such are $M_{23}C_6$ are found at lath boundaries and PAGBs and vanadium nitrides can also be found at the boundaries or within the grains [4, 27-29]. Other precipitates in HT9 reported by Kai et al. are equiaxed and elongated $M_{23}C_6$, MX platelet and needle-like M_2X [23]. The large carbides are $M_{23}C_6$ rich in Cr, Mn, W, V, and Si

whereas the vanadium nitrides are smaller 20-40 nm [4]. The different precipitate types and morphologies are found in specific regions of the HT9 where the structure varies. The $M_{23}C_6$ can be found in tempered martensite and the lath boundaries, the MX is found in tempered martensite and the M_2X is found in ferrite regions of the HT9 [2]. The crystal structures and lattice constant for the different types of precipitates can be seen below in table 2.2.2.1 [2].

Table 2.2.2.1: Crystal structure and lattice constant for HT9 precipitates [2].

Precipitate	Crystal Structure	Lattice Constant a [nm]	Lattice Constant c [nm]
Equiaxed $M_{23}C_6$	FCC	1.06	N/A
Elongated $M_{23}C_6$	FCC	1.06	N/A
MX	FCC	0.42	N/A
M_2X	HCP	0.27	0.44

Not all these phases are in equilibrium but these are the possible phases that can be observed through the heat treatment process [2]. This is why only $M_{23}C_6$ and MX only some of the precipitates times are present in the chemi-STEM maps in figure 2.2.2.3. As noted earlier with the heat treatment of our sample, it is tempered martensite, which also the types of precipitates observed the $M_{23}C_6$ and the MX. M_2X precipitates have been seen in ion irradiated CNS (China Nuclear Steel) II which is nominally 12-Cr at 460 °C with very high doses up to 450 dpa [30]. This would suggest that as the dose reaches very high levels the further from phase equilibrium the microstructure is.

The initial microstructure of HT9 is martensitic steel with packets of lath grains inside of the prior austenite grain boundaries. The average grain size is 542 ±7 nm calculated by using 94 grains. The way the size is determined is to trance the grain boundaries on the image in the software called WRITEit on a laptop with a touch screen. The touch pen is used to trace the images on the original image. Then the background is made opaque and then the image is saved

again. Then the image is imported into imageJ [31] and the size is measured by first turning the image into an 8-bit image then use Binary-make binary tool to make the image binary and then inverting the image and then measuring the scale bar with the line tool to let imageJ the length to pixel ratio. Following this analyze-analyze particle the area for each grain is collected. Then finding the diameter using equation 2.2.2.1 and then averaging the diameters from each grain. Figure 2.2.2.1 shows the grains and the marked grains along with the area distribution of each grain seen in figure 2.2.2.1.C.

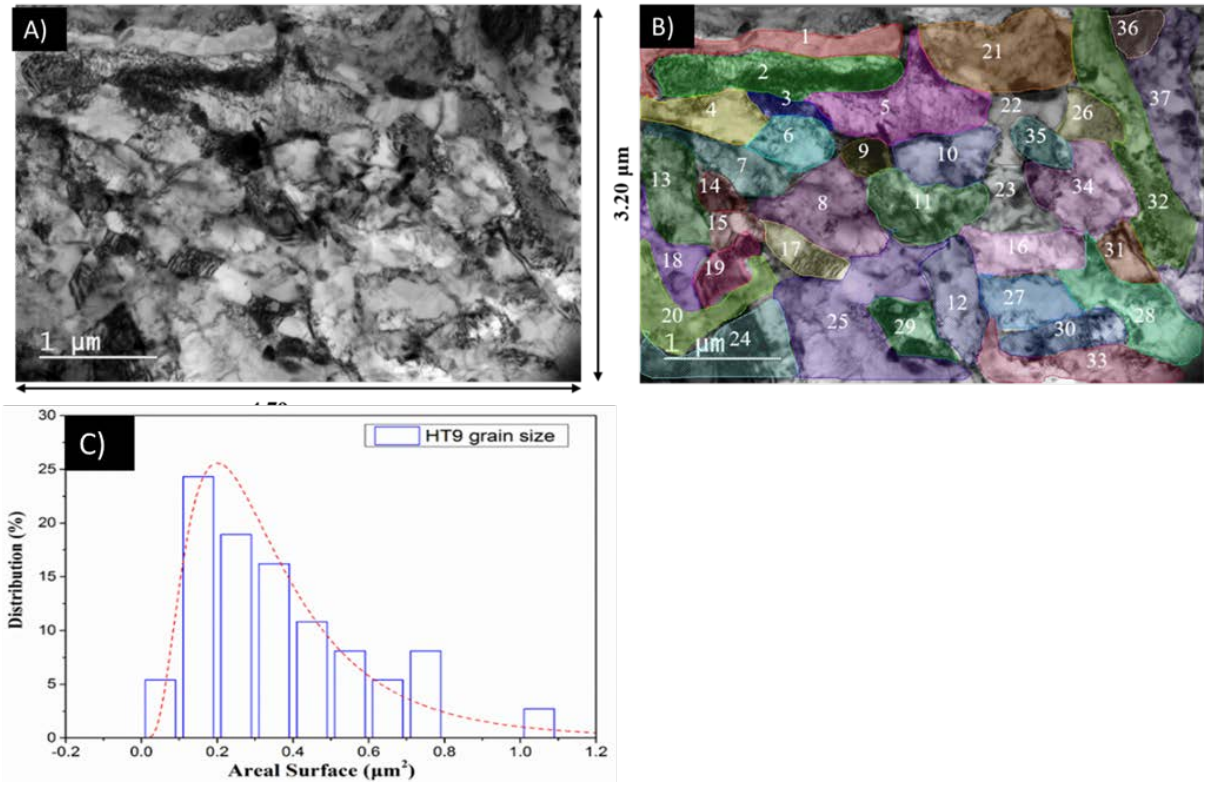

Figure 2.2.2.1: Grain boundary of initial HT9. A) shows the image used to calculate grain size and B) shows the marked grains on the image. C) shows the surface area histogram of the area of the grains [3].

$$D = \sqrt{\frac{4A}{\pi}} \qquad 2.2.2.1$$

The martensitic lath structure of HT9 can be seen in figure 2.2.2.2 which shows a variety of areas from a FIB lift-out.

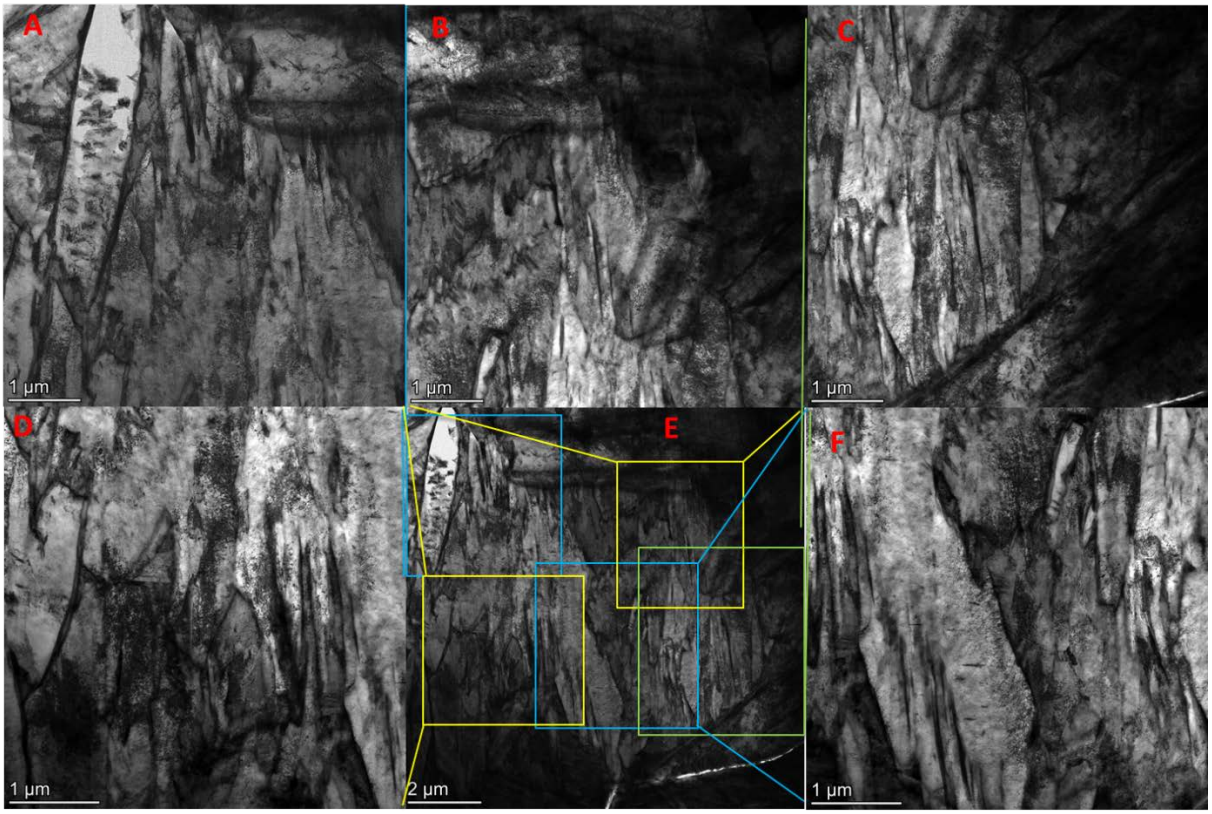

Figure 2.2.2.2: Martensitic lath boundaries of HT9.

The precipitates that can be found in as received HT9 martensitic steels are $M_{23}C_6$ carbides and small vanadium rich nitrides. These can be seen within the grains and along the lath boundaries and the larger carbides are also seen on prior austenite grain boundaries. An example of these can be seen below in figures 2.2.2.3-2.2.2.4[4], where figure 2.2.2.3 shows the chemi-STEM image showing both $M_{23}C_6$ carbides and the vanadium rich nitrides. Figure 2.2.2.4 shows an atomic probe tomography also confirming the presents of both the $M_{23}C_6$ carbides and the vanadium rich nitrides.

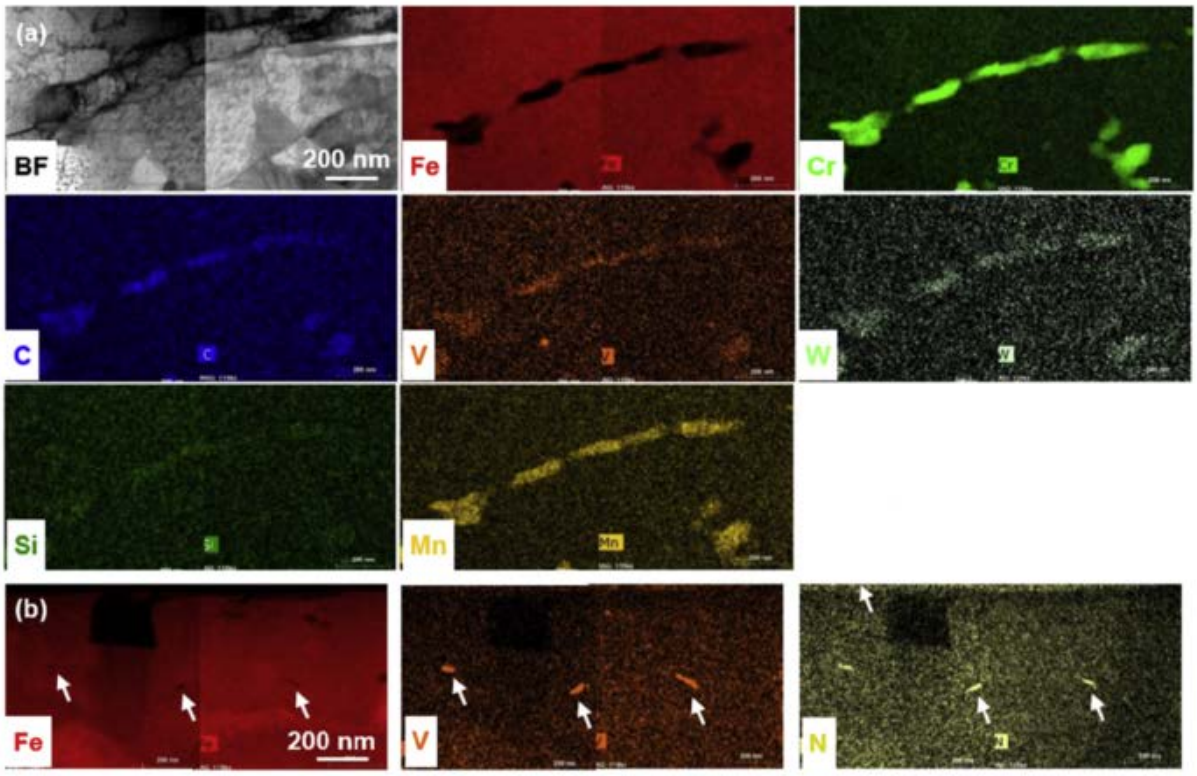

Figure 2.2.2.3: Chemi-STEM map of as received HT9 sample. A) shows the $M_{23}C_6$ carbides present in the initial microstructure while B) shows the vanadium rich nitrides [4].

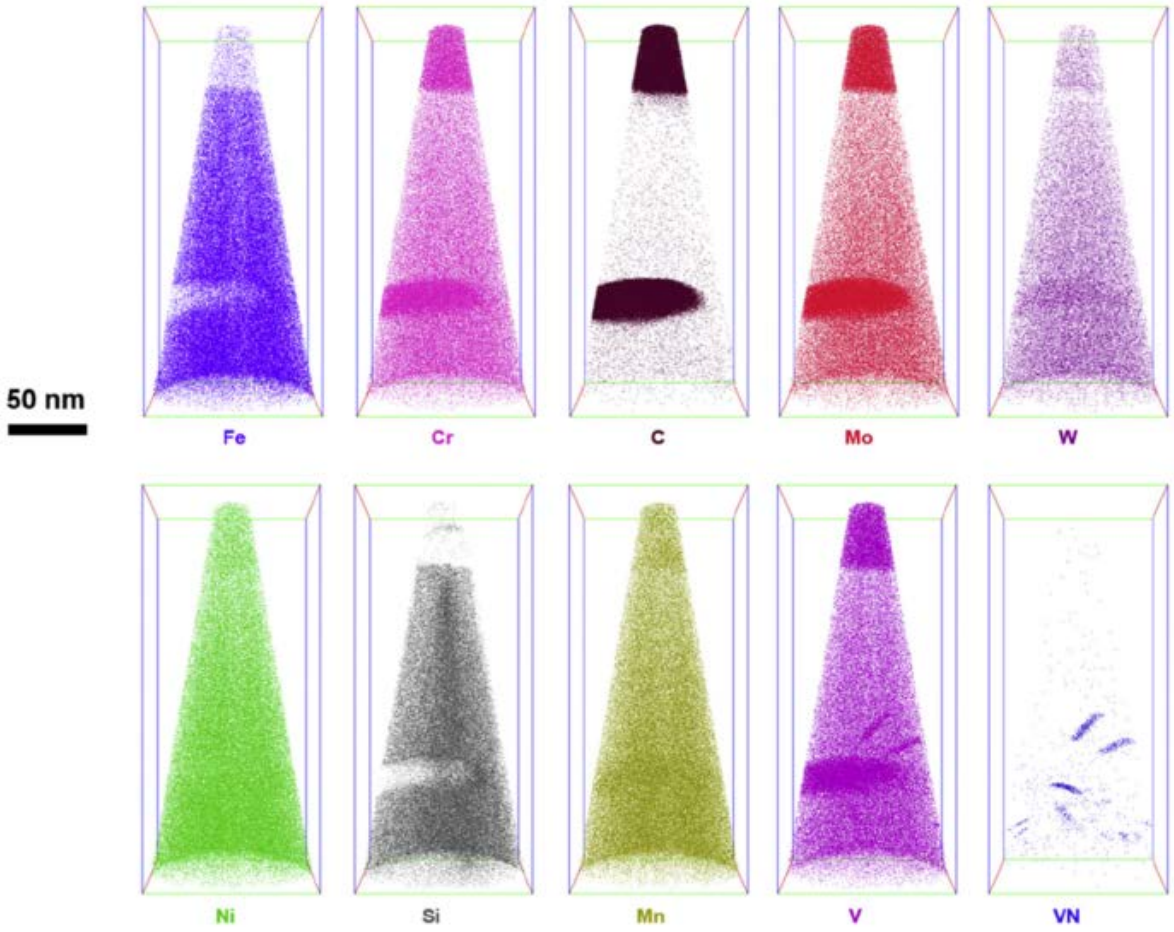

Figure 2.2.2.4: ATP of as received HT9 sample showing both the presents of $M_{23}C_6$ carbides and vanadium rich nitrides [4].

2.3 Irradiation Experiments

2.3.1 Irradiation Facility

The facility that was used to irradiate the samples is the Tecnai G^2 20 Twin microscope at the JANNuS-Orsay dual-beam TEM facility [32]. In this facility the samples can be irradiated in situ with 4 MeV Au^{2+} ions and simultaneously implanted with 10 keV He^+ ions. The tiling of the stage in the JANNuS facility was such that the surface normal of the sample made a 22° angle with the helium beam and 23° angle with the ion beam as the two accelerators are 45° degrees apart [33].

There were four experiments done over 5 days. There was a sequential experiment where the Helium was implanted then the sample was irradiated with gold ions with in-situ observation under the microscope. Along with the sequential study, three dual-beam studies were conducted at different Helium to dpa ratios including 2.2, 22 and 100 appm He/dpa. For the sequential case the final appm He per dpa would be equivalent to 22 if they were done at the same time. Table 2.3.1.1 below shows the flux and fluences for both the gold ion and Helium ions along with the dose rate, helium implantation rate and duration of irradiation and observation.

Table 2.3.1.1: Experimental Conditions.

	He Flux [ions/cm^2/s]	He implantation rate [appm/s]	He fluence [ions/cm^2]	dpa/s	Au Flux [ions/cm^2/s]	Au fluence [ions/cm^2]
Sequential implantation	$3.00x10^{10}$	$3.54x10^{-2}$	$3.17x10^{13}$	$1.61x10^{-3}$	$4.05x10^{11}$	$4.27x10^{15}$ (17 dpa)
100 He appm/dpa	$1.40x10^{11}$	$1.65x10^{-1}$	$1.44x10^{15}$ (at 17 dpa)	$1.65x10^{-3}$	$4.15x10^{11}$	$4.27x10^{15}$ (17 dpa)
22 He appm/dpa	$3.00x10^{10}$	$3.54x10^{-2}$	$3.17x10^{14}$ (at 17 dpa)	$1.61x10^{-3}$	$4.05x10^{11}$	$4.27x10^{15}$ (17 dpa)
2.2 He appm/dpa	$3.00x10^{9}$	$3.54x10^{-3}$	$3.17x10^{14}$ (at 17 dpa) $6.33x10^{13}$ (at 34 dpa)	$1.61x10^{-3}$	$4.05x10^{11}$	$4.27x10^{15}$ (17 dpa) $8.54\ x10^{15}$ (34 dpa)

In all cases, the samples were observed for four hours but the time of irradiation varied depending on the target rate of appm He/dpa. All experiments were carried out in one day with the exclusion of the 100 appm He per dpa dual-beam experiment which is the last row of data in table 2.3.1.1, which was an overnight experiment.

The damage produced by the implantation of helium and irradiation by gold ions were calculated using SRIM [10] in quick mode using 40 eV and 28 eV for Fe and C respectably. The displacements caused by the helium ions were two to three orders of magnitude smaller than the

displacements caused by the gold ions thus they are negligible, this can be seen in figure 2.3.1.1.B. The implantation depth of both the gold and helium ions can be seen below in figure 2.3.1.1 which shows the SRIM calculations [10].

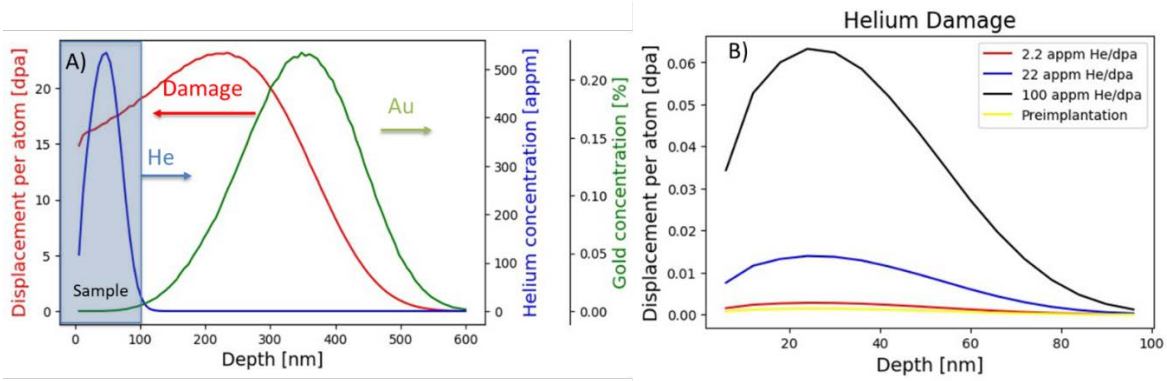

Figure 2.3.1.1: SRIM calculation for implantation depth into the HT9 samples by the 10 keV He^{+} and 4 MeV Au^{2+} ions. A) shows the damage profile of the gold ions, the percentage gold and the helium concentration for the entire range of gold and the sample thickness while B) shows the damage induced by the implantation of helium.

What can be observed is that all the helium is implanted in the first 100 nm, which is the thickness of the sample while the gold ions do not implant in this thickness as seen in figure 2.3.1.1.A. As seen in the SRIM calculations they would only begin to implant after 100 nm, which would only come into effect with a thicker sample. This shows that gold ions are only used to induce damage while helium ions do not induce damage but are instead implanted into the sample.

2.4 Method for Bubble Measurements

2.4.1 Imaging/detection of the bubbles

The method for counting helium bubbles is to observe them under TEM bright-field. There are two classes of bubbles, those that can be seen in a focused bright-field image and those that cannot. When the TEM is at focus there is a minimum size requirement to be visible and that

is a diameter of 5 nm or larger then they can be viewed under dynamical or bright-field kinematical conditions [34]. For any bubble that is smaller than about 5 nanometers they will not appear in a focused TEM image. The way to make them appear is to take TEM images in either under- or over-focused conditions. Counting the cavities so not as simple as it sounds there is an oxide film that forms which worsens image quality as dose irradiation damage. The bubbles appear in the out-of-focus conditions due to phase-contrast and weak absorption. This phase shift is also the cause of Fresnel fringes [34]. Fresnel fringes cause the over-focused image to have a white ring around the black bubble and in the under-focused it caused a black ring to appear around the white bubble [34]. To count the number of bubbles on the images the software ImageJ is used to analyze to bubble size. In this software using the line tool, the scale bar is measured and then the program is told what the actual length is and from this, the program can find a pixel to length ratio. Within the ImageJ software all the bubbles are traced with the elliptical or oval tool whichever allowed for better fit only. Both the under- and over-focused images are used to compare if each white bubble on the under focused has a corresponding dark bubble on the over-focused. Only the white portion of the bubbles are marked, the edge between the white bubble and the first dark fringe. If there is uncertainty in the size due to the instrument limitations or uncertainty in the bubble itself, it was noted on the measurement sheet.

2.4.2 Bubble density measurements

The densities were calculated by finding the number of bubbles in the measured area. The area can be found from ImageJ and the density was measured. Two density values are calculated one that was the number of certain bubbles divided by the volume, which is the lower end of the error bar. The upper limit on the error bar is the total number of observed bubbles divided by the volume.

2.4.3 Bubble size measurements

The bubble size is measured by ImageJ when the bubbles are marked with the elliptical tool. The output of ImageJ included area and the major/minor axis. From the major and minor axis, the equivalent diameter can be calculated using equation 2.4.3.1 which is based on equivalent disc surface area. The average sizes are reported for certain bubbles and the total bubbles.

$$d = \sqrt{d_{major} * d_{minor}} \qquad 2.4.3.1$$

There is an error intrinsic to the resolution of the image but there is also error associated with measuring the bubbles. The error on the bubble size can is 10 percent of the measured size when measuring to the inner edge of the first dark Fresnel fringe on an under focused image [34].

2.4.4 Correction for different defocus amounts

One issue that occurred was that, not all the images had the same defocus value they varied from 500 nm to 2 μm. The different defocus values change the size of the Fresnel fringes, which could induce more error by overestimating some bubbles compared to others. As the defocus value increases the larger the Fresnel fringes become, the easier it is to measure the size incorrectly. To account for this the parameter β can be held constant in equation 2.4.2.1[34] and then solve for the ratio of the different measured void ratios (r_0) seen in equation 2.4.2.2.

$$\beta = \frac{\Delta f}{\pi k_0 r_0^2} \qquad 2.4.2.1$$

$$\frac{r_{0_1}}{r_{0_2}} = \sqrt{\frac{\Delta f_1}{\Delta f_2}} \qquad 2.4.2.2$$

Δf is the defocus value

K_0 is the electron wavevector [λ^{-1}]

With these equations, the sizes of the bubbles from the same experimental sequence can be compared. All the adjustments were made to make Δf_1 equal to -1µm to find the effective bubble size radius for comparison. In this study, the incident electron beam was constant so k_0 remained constant.

Chapter 3:

Experimental Results

In this study, the effect of the order, sequential irradiation or dual-beam and the effect of the appm He per dpa are studied on HT9. The results gathered for the counting can be seen below in table 3.1.1 which shows the average bubble size and the bubble density for each experiment. Within the table NO is given for no observation.

Table 3.1.1: Bubble size and density.

Dual/ Sequential	Name	Total Counts	Average size [nm]	dpa	density [10^{23} m^{-3}]	Temperature [°C]	He appm/dpa
He then ion	0 dpa 221 appm He	NO	NO	0	NO	430	sequential irradiation
	0 dpa 331 appm He	115	1.8±0.2	0	0.34±0.05		
	10 dpa 331 appm He	222	1.9±0.2	10	0.69±0.07		
	15 dpa 331 appm He	350	1.8±0.2	15	1.15±0.08		
Dual	15 dpa 33 appm He	NO	NO	15	NO	430	2.2
	20 dpa 44 appm He	NO	NO	20	NO		
	26 dpa 57.2 appm He	NO	NO	26	NO		
	31 dpa 68.2 appm He	302	2.1±0.2	31	1.88±0.2		
Dual	15 dpa 330 appm He	177	2.4±0.2	15	0.6±0.03	430	22
	20 dpa 440 appm He	220	2.1±0.2	20	0.74±0.03		
	26 dpa 572 appm He	253	2±0.2	26	0.8±0.09		
Dual	10 dpa 1000 appm He	230	1.7±0.2	10	1.75±0.29	430	100
	20 dpa 2000 appm He	400	1.3±0.1	20	2.98±0.58		
	26 dpa 2600 appm He	528	1.5±0.1	26	4.43±0.26		

The dpa ranged from 0 to 31 while the amount of added Helium was between 33 and 2600 appm Helium with all the experiments carried out at 430°C.

3.1 Sequential Experiment

In the sequential experiment, first, the sample of HT9 was implanted with Helium at 430 °C then it was observed. This can be seen in figure 3.1.1 where bright-field images are showing the same area for 221 appm He and 331 appm.

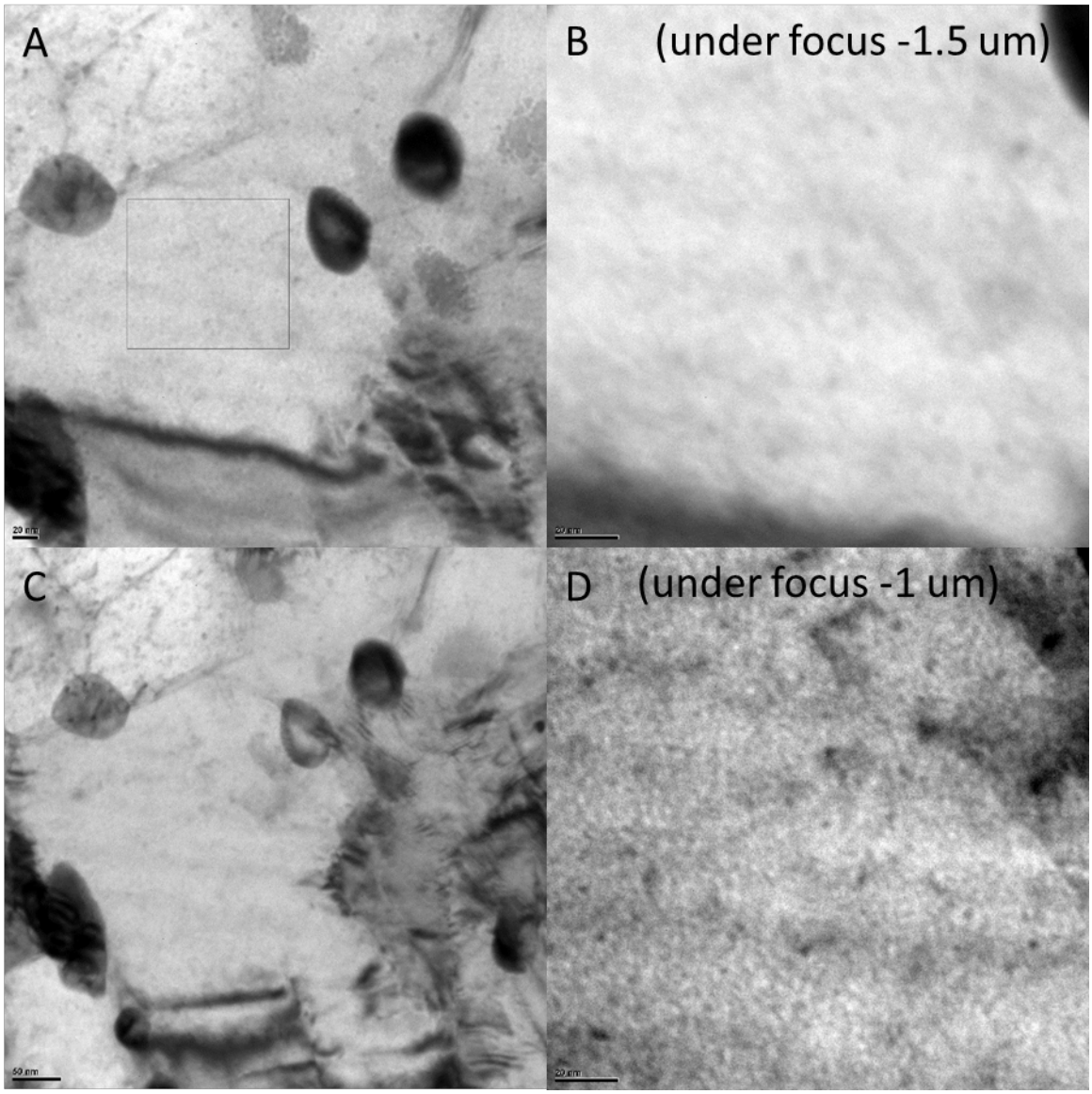

Figure 3.1.1: TEM bright-field images of sequential implantation of helium then gold ions.

What can be observed here is that under 0 dpa and 221 appm He there are no cavities that are formed by the helium implantation. This is different if 100 appm He is added as seen in figure 3.1.1.D where there are bubbles present.

The corresponding under-focused and over-focused images for the sequential irradiation experiment of 0 dpa and 221 appm He, 0 dpa 331 appm He, 10 dpa 331 appm He and 15 dpa 331

appm He can be seen below in figure 3.1.2 along with the number of bubbles observed in each case.

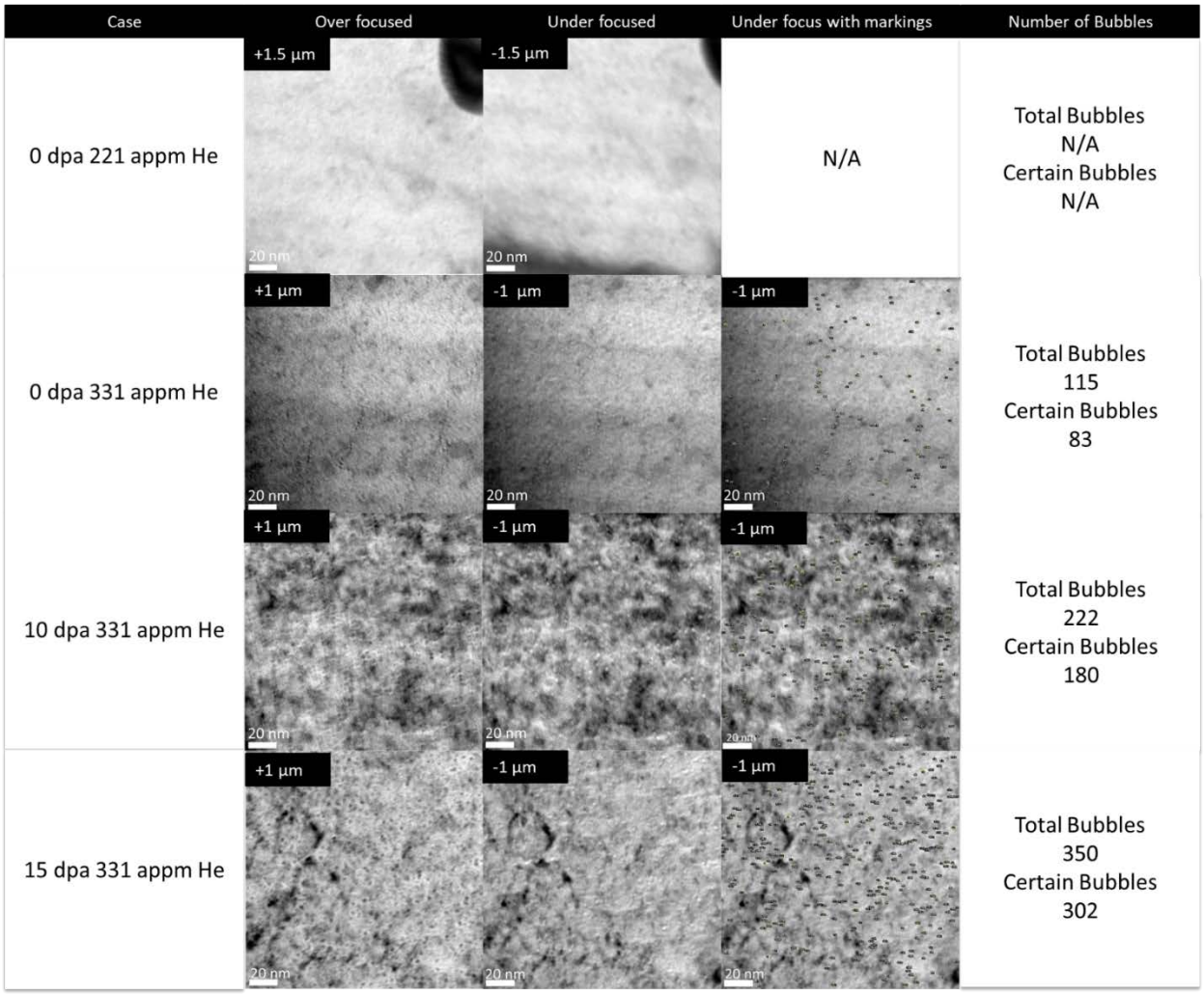

Figure 3.1.2: Sequential implantation of first 10 keV helium atoms followed by 4 MeV gold ions.

What can be observed in figure 3.1.2 is that a threshold for bubble formation occurs between 221 appm and 331 appm helium. The overall trends of the sequential implantation experiment can be seen in figure 3.1.3 which shows the bubble size vs dpa; figure 3.1.4 shows the bubble size distribution and figure 3.1.5 shows the bubble density vs dpa.

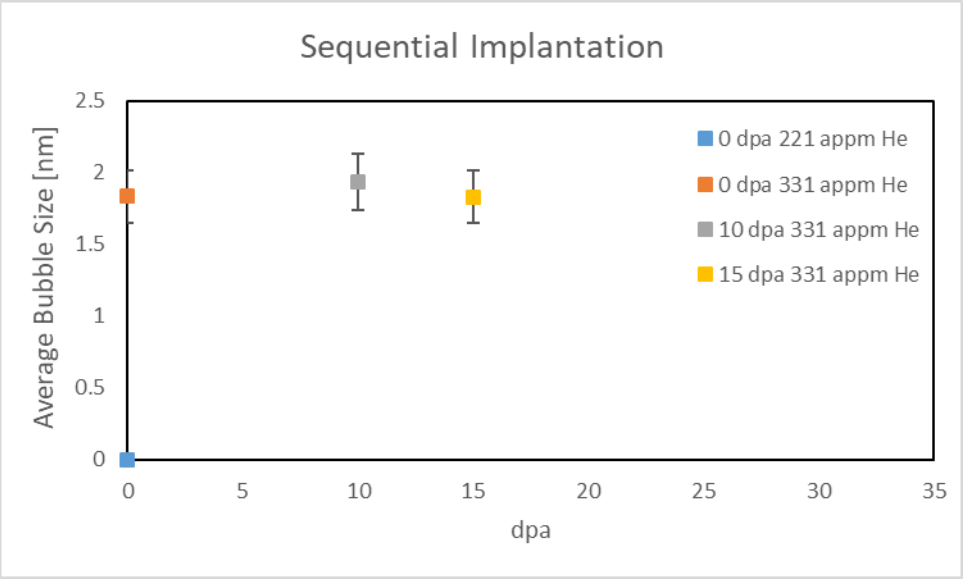

Figure 3.1.3: Sequential implantation of helium then gold irradiation at 430 °C showing the bubble size vs the dpa.

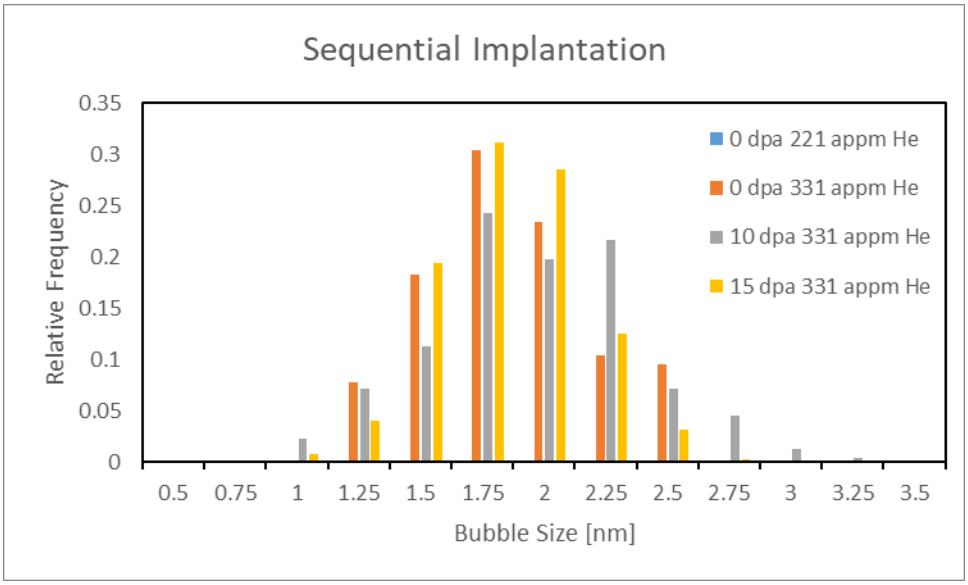

Figure 3.1.4: Sequential implantation of helium then gold irradiation at 430 °C showing the size distribution.

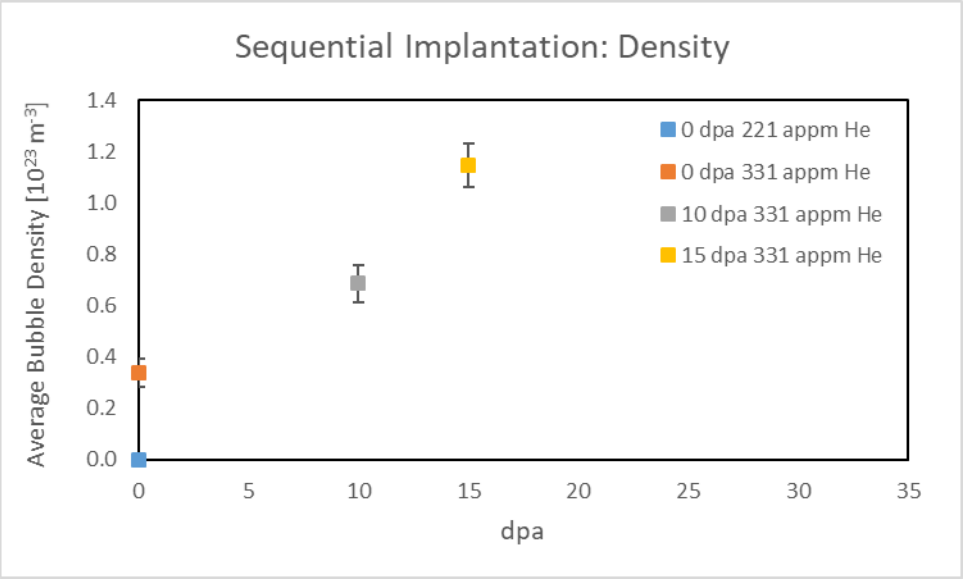

Figure 3.1.5: Sequential implantation of helium then gold irradiation at 430 °C showing the bubble density vs the dpa.

What can be observed from these figures is that at first the bubble size remains constant over all the dpa ranges; this can be observed in figures 3.1.3 and 3.1.4. The addition of irradiation damage to the pre-implanted HT9 causes a shift in the size distribution to grow larger. The overall amount of helium has increased in HT9 and this can be seen in figure 3.1.5 where the overall density continued to increase as the dpa increase and the implanted quantity of helium increases.

3.2 Dual-beam irradiation with 2.2 helium appm/dpa

In this experiment, the implanted helium was 2.2 appm per dpa with 15 dpa 330 appm He, 20 dpa 44 appm He, 26 dpa 57.2 appm He and 31 dpa 68.2 appm He are seen in figure 3.2.1. In this experimental set, very few bubbles were observed as seen in figure 3.2.1 only the last case of 31 dpa and 68.2 appm He had bubbles.

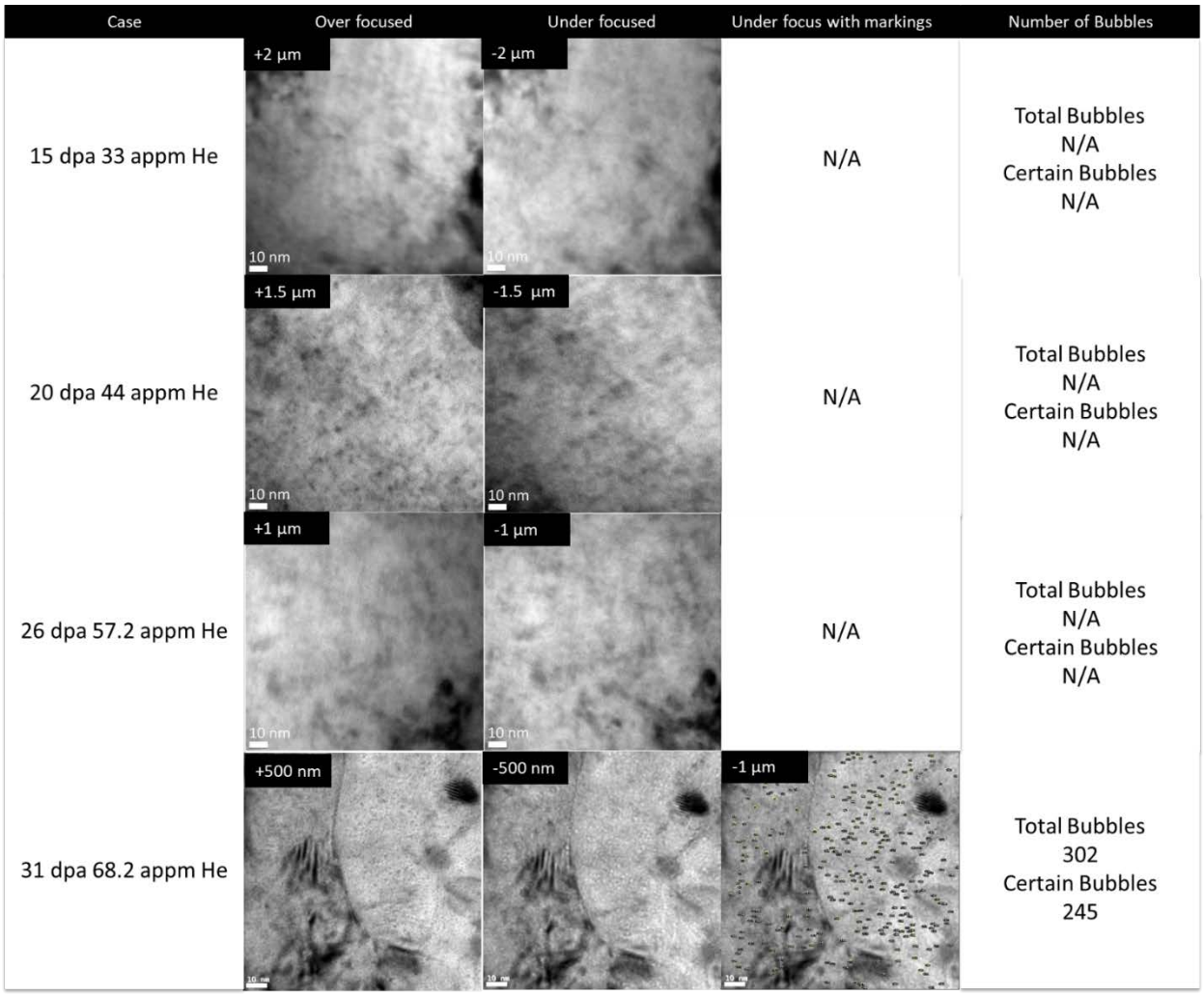

Figure 3.2.1: Dual-beam implantation of helium and gold ions for 15 to 31 dpa and 33 to 68.2 appm He with the number of certain and total bubbles for each dose step. The helium appm/dpa ratio was 2.2.

What can be observed is that there are no bubbles present until 31 dpa and 68.2 appm He. Bubbles were attempted to be observed as the magnification is larger than the other cases and the larger defocus would make the fringes larger allowing the smaller bubbles to be visible. The dose level of 31 dpa and 68.2 appm He was used to see if bubbles would form at a larger dose since it did not between 15 and 26 dpa with their respective helium concentration. The summary plots can be seen in figure 3.2.2-3.2.4 and they show the bubble size vs dpa, size distribution vs. dpa

and bubble density vs dpa. The only potential comment would be a required threshold as only the highest dpa and helium implanting of 31 dpa and 68.2 appm He had observable bubbles.

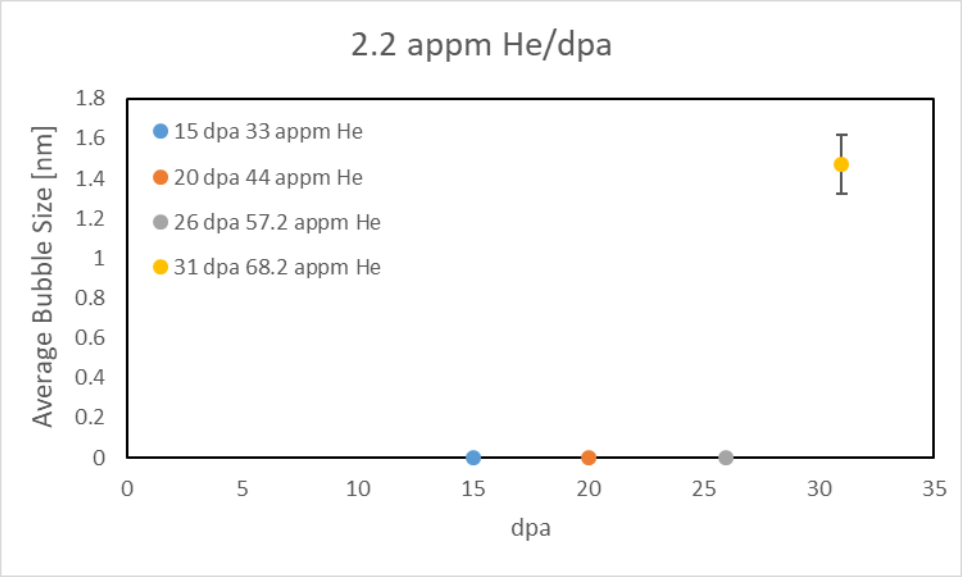

Figure 3.2.2: Dual-beam irradiation with Helium and gold ions at a rate of 2.2 appm He per dpa at 430 °C showing bubble size versus the dpa.

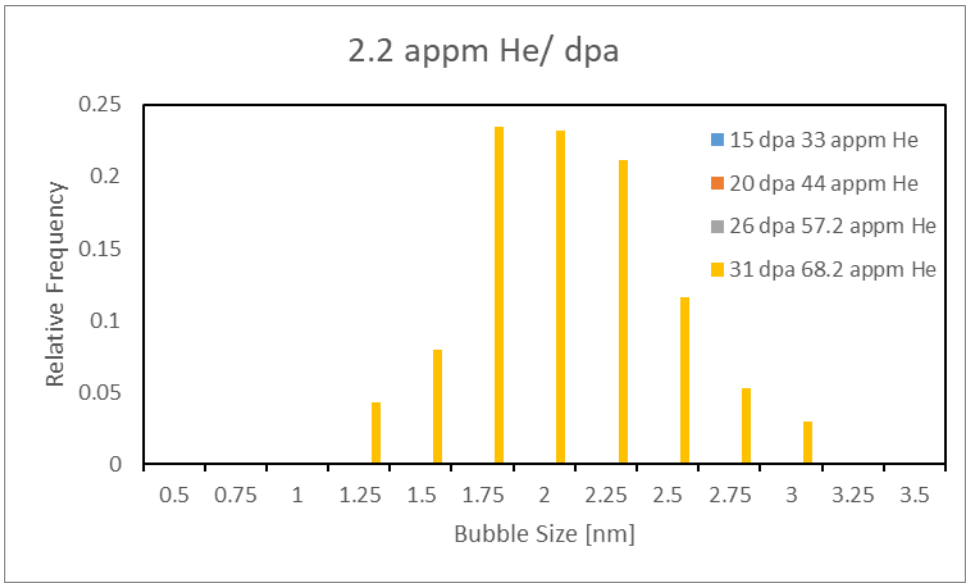

Figure 3.2.3: Dual-beam irradiation with Helium and gold ions at a rate of 2.2 appm He per dpa at 430 °C showing size distribution.

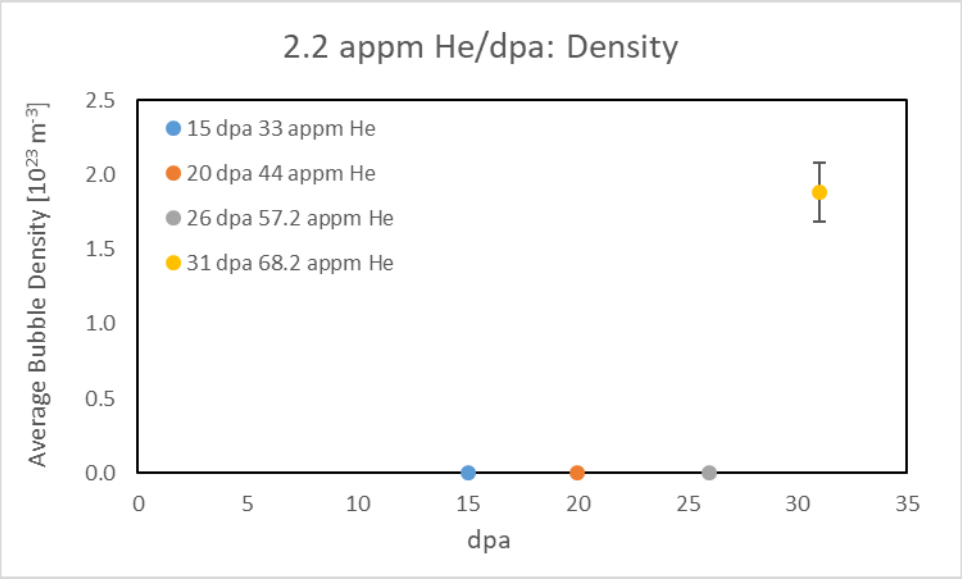

Figure 3.2.4: Dual-beam irradiation with Helium and gold ions at a rate of 2.2 appm He per dpa at 430 °C showing bubble density versus the dpa.

3.3 Dual-beam irradiation with 22 helium appm/dpa

In this experiment, the implanted helium was 22 appm per dpa at 15 dpa 330 appm He, 20 dpa 440 appm He and 26 dpa 572 appm He. Bubbles were observed at all conditions as seen in figure 3.3.1.

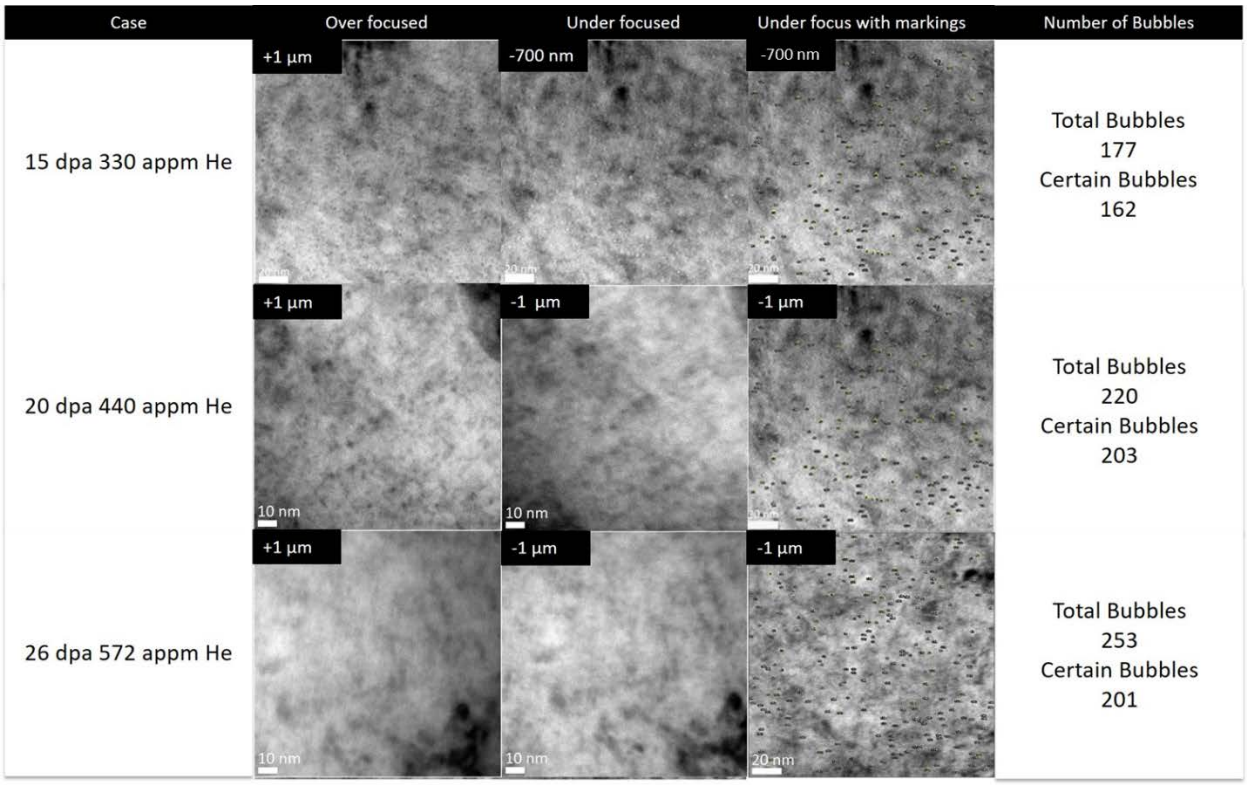

Figure 3.3.1: Dual-beam implantation of helium and gold ions for 15 to 31 dpa and 33 to 68.2 appm He with the number of certain and total bubbles for each dose step. The helium appm/dpa ratio was 22.

What can be observed in this case is that all cases had bubbles unlike 2.2 appm He/dpa.

The group's trends can be seen in figure 3.3.2-3.3.4, which shows the bubble size vs dpa, size distribution vs dpa and the bubble density vs dpa. The size of the bubbles is decreasing but remaining within the error of each other. However, there is a shift in the size distribution to the left as seen in figure 3.3.3.

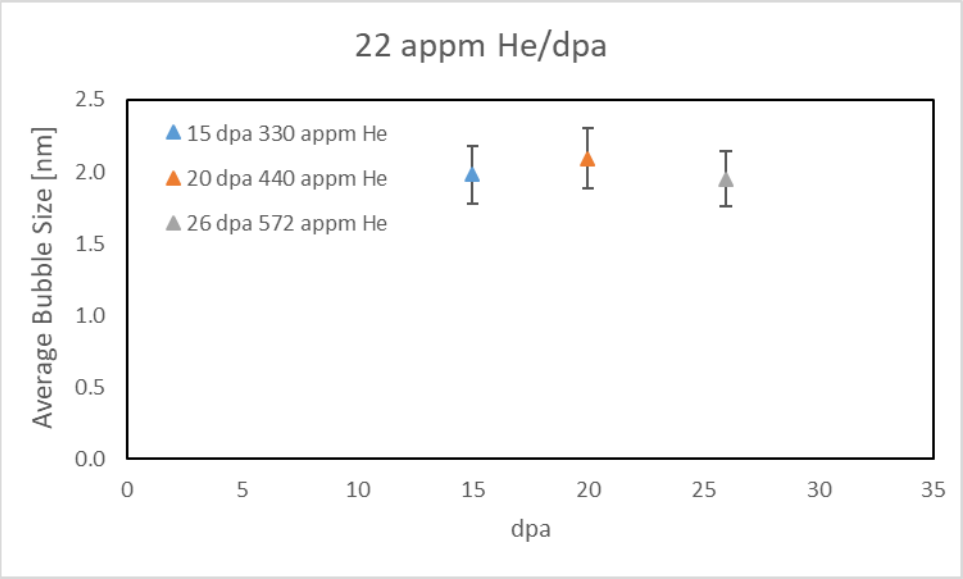

Figure 3.3.2: Dual-beam irradiation with Helium and gold ions at a rate of 22 appm He per dpa at 430 °C showing bubble size versus the dpa.

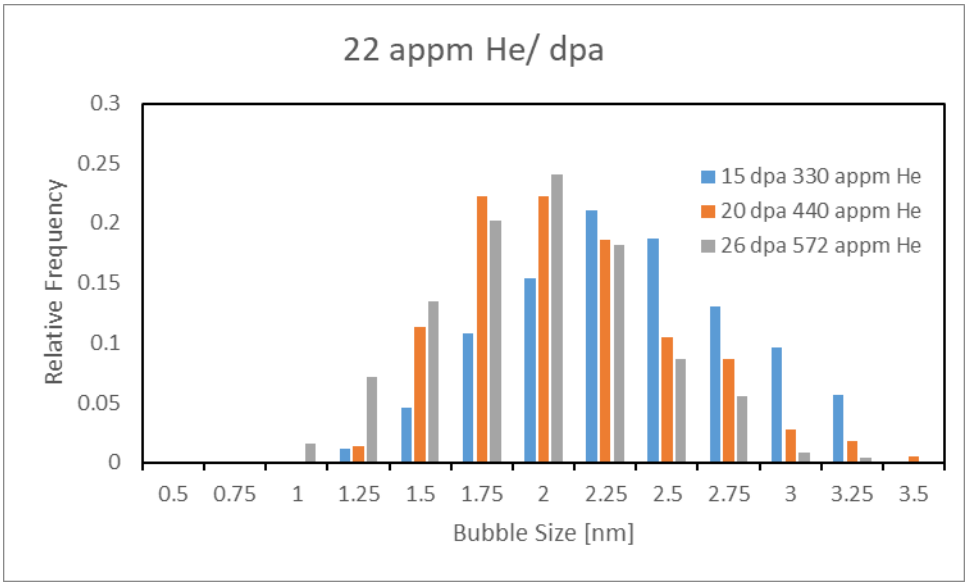

Figure 3.3.3: Dual-beam irradiation with Helium and gold ions at a rate of 22 appm He per dpa at 430 °C showing size distribution.

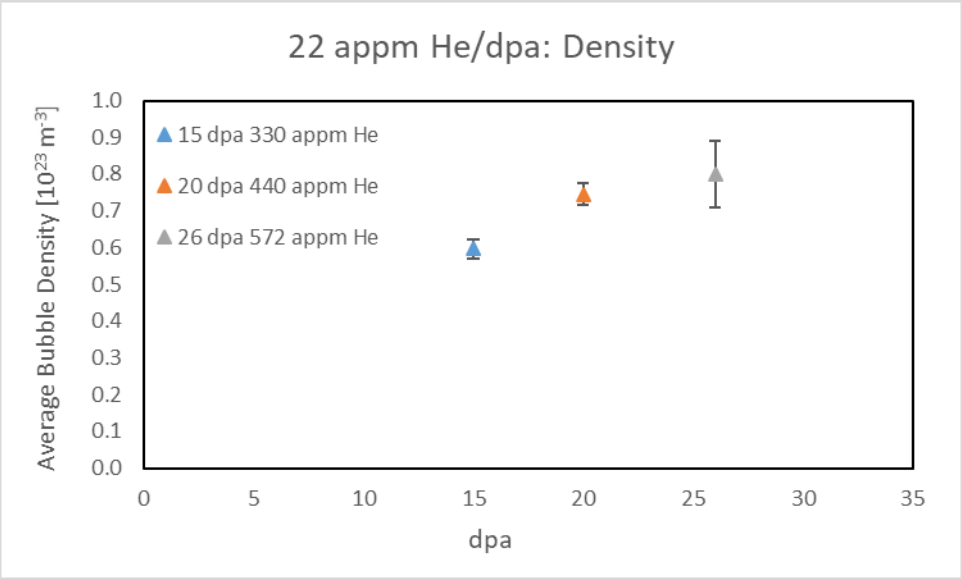

Figure 3.3.4: Dual-beam irradiation with Helium and gold ions at a rate of 22 appm He per dpa at 430 °C showing bubble density versus the dpa.

The observable trend is the density of the bubbles continues to increase with dose and implanted helium concentration.

3.4 Dual-beam irradiation with 22 helium appm/dpa

In this experiment, the implanted helium was 100 appm per dpa for 10 dpa 1000 appm, 20 dpa 2000 appm, and 26 dpa and 2600 appm. Bubbles were observed in this experimental set as seen in figure 3.4.1. This was the only overnight experiment. In this experiment, all cases had bubbles present.

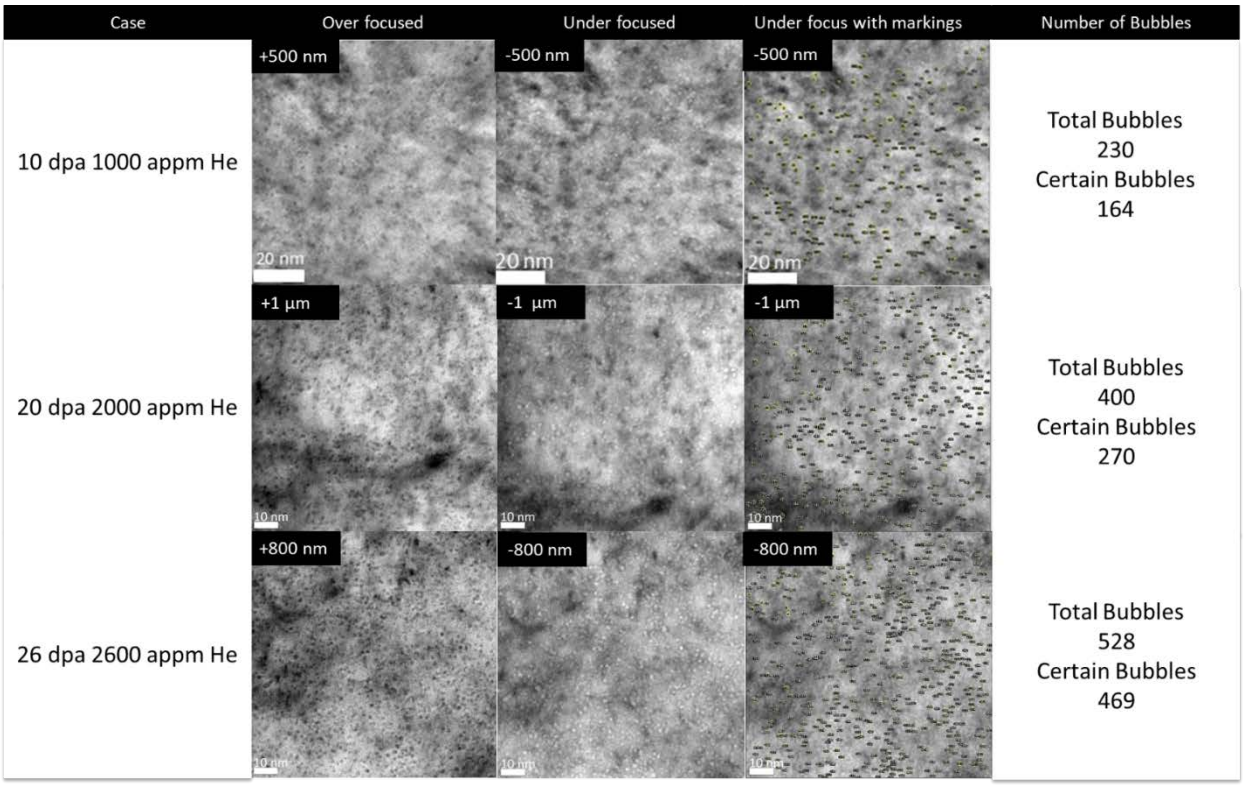

Figure 3.4.1: Dual-beam implantation of helium and gold ions for 15 to 31 dpa and 33 to 68.2 appm He with the number of certain and total bubbles for each dose step. the helium appm/dpa ratio was 100.

The group's trends can be seen in figure 3.4.2-3.4.4, which shows the bubble size vs dpa, relative frequency vs bubble size and the bubble density vs dpa. The trend that can be seen that the bubble size seems to be slightly decreasing but remaining within error bars this can be seen in figure 3.4.4 and figure 3.4.5.

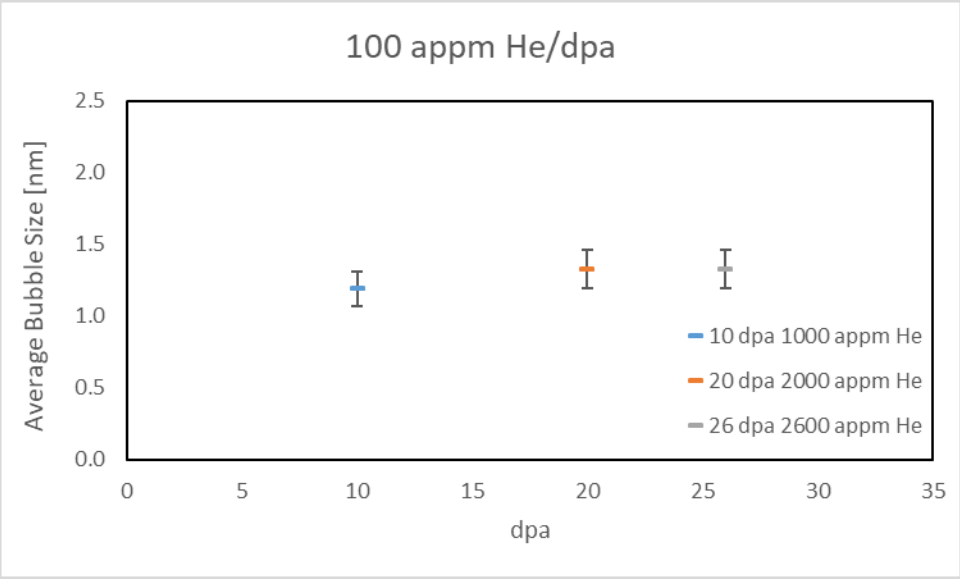

Figure 3.4.2: Dual-beam irradiation with Helium and gold ions at a rate of 100 appm He per dpa at 430 °C showing bubble size versus the dpa.

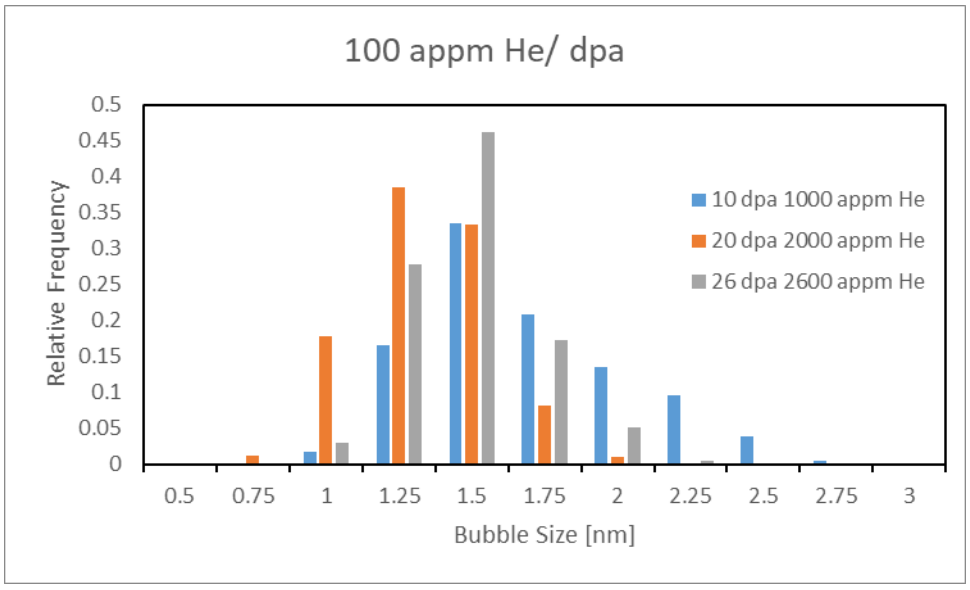

Figure 3.4.3: Dual-beam irradiation with Helium and gold ions at a rate of 100 appm He per dpa at 430 °C showing size distribution.

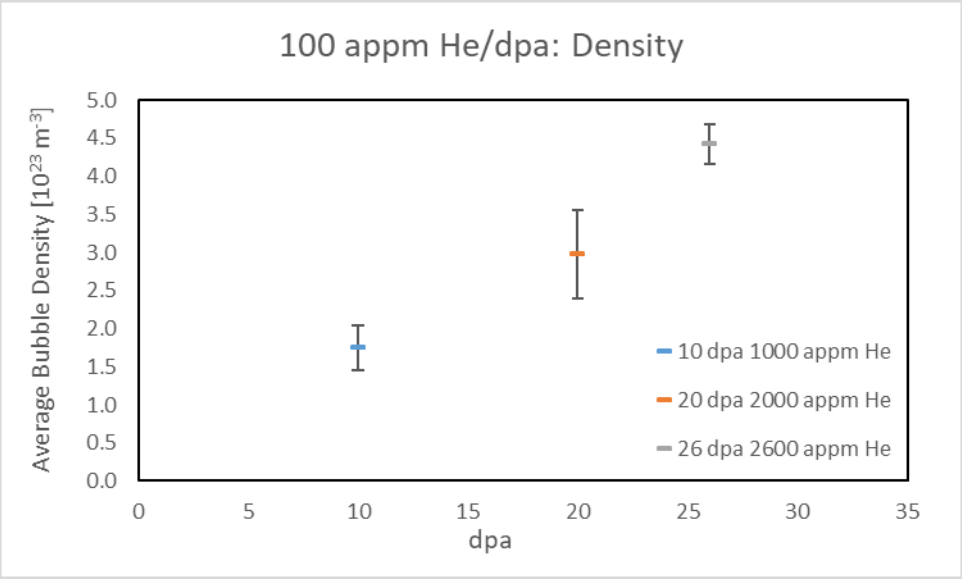

Figure 3.4.4: Dual-beam irradiation with Helium and gold ions at a rate of 100 appm He per dpa at 430 °C showing bubble density versus the dpa.

The trends are the same as the other cases the bubble size decreases but remain within error bars of each other. The density increase as the dpa increase and the trends appears to be linear as seen in figure 3.4.4.

3.5 Comparisons between cases

Comparing the data collected between the sequential implantation and the dual-beam exponent there is some overlapping data. At 15 dpa, 330 appm He (dual-beam) and 15 dpa 331 appm He (sequential implantation) they both have the same effective 22 appm He per dpa. The data collected from this experiment can be seen below in figure 3.5.1-3.5.3.

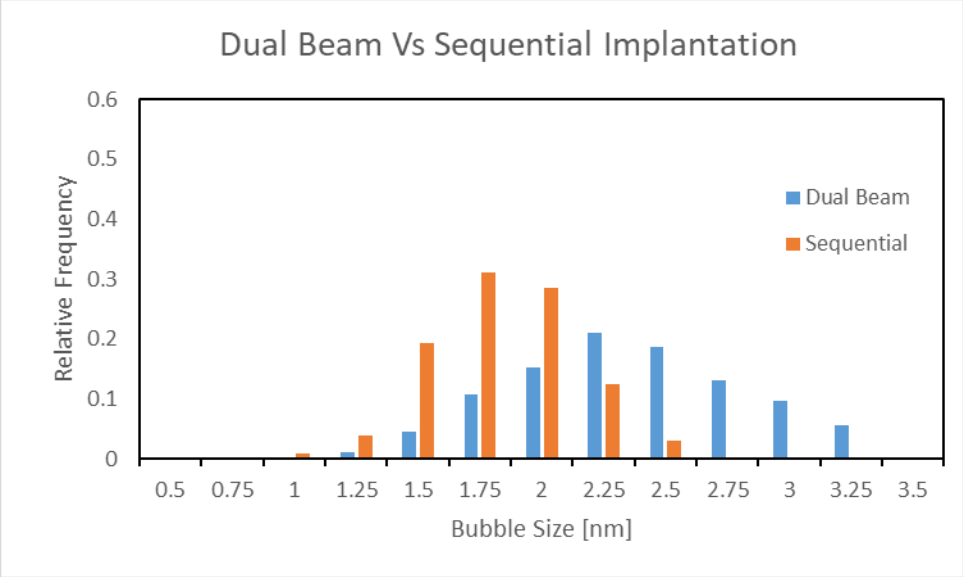

Figure 3.5.1: Comparing the size distribution of dual-beam and sequential implantation.

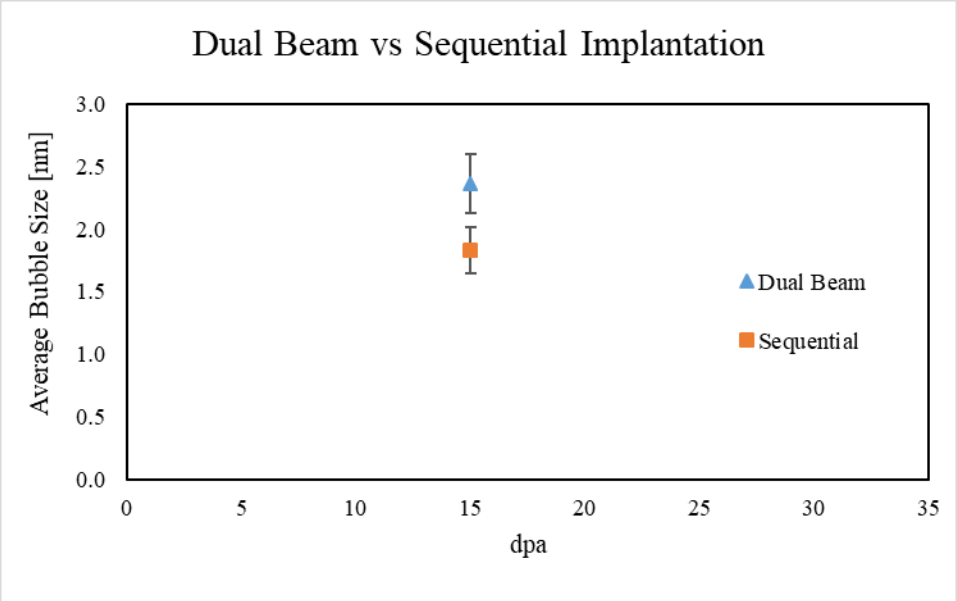

Figure 3.5.2: Average bubble size for both dual-beam and sequential implantation study with 15 dpa and ~330 appm He.

The trend that can be seen in figure 3.5.1 and figure 3.5.2 is that as dual-beam produces bubbles with larger sizes then pre-implantation of helium followed by gold irradiation.

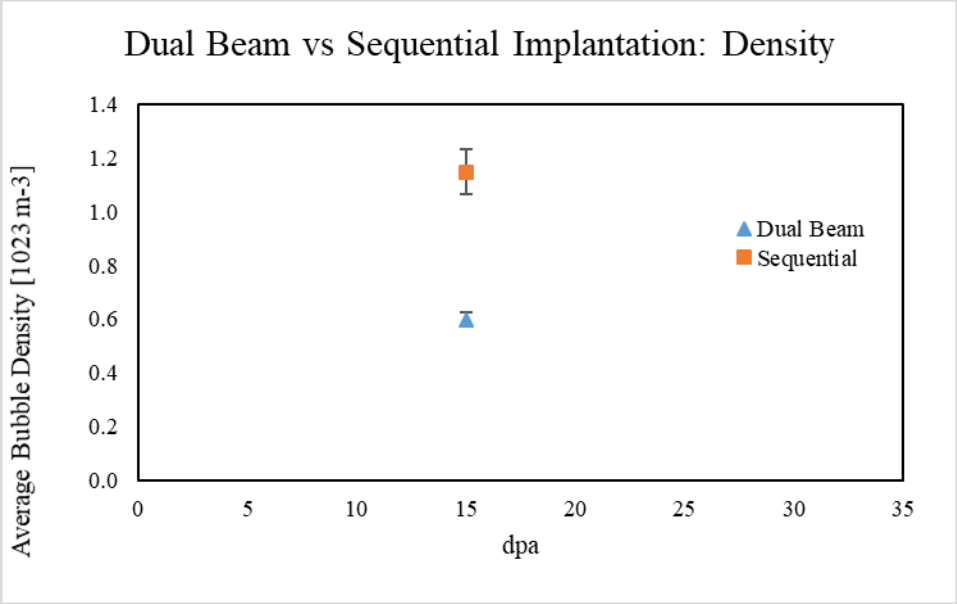

Figure 3.5.3: Shows the density for the dual-beam and sequential study at 15 dpa and ~330 appm He.

The trend that can be seen here is that sequential implantation creates more bubbles.

Table 3.5.1 below shows the results when comparing dual-beam versus sequential implantation.

Table 3.5.1 Dual-beam vs Sequential implantation, showing the density and average bubble size for dual-beam 15 dpa and 330 appm He and the sequential for 15 dpa and 331 appm He.

Dual-Beam vs Sequential	Bubble Size [nm]	Bubble Density [Bubble $*10^{23}/m^3$]
Dual-Beam	2.4±0.2	0.6±0.03
Sequential	1.8±0.2	1.2±0.08

The influence of different rates on implanting helium was also studied during the dual-beam experiments. Figure 3.5.4 shows the average bubble size while figure 3.5.5 shows the average density. The trend that can be gathered from there figures is that the bubble size decreases as the rate of helium implantation increase once bubbles are formed this can be seen in

figure 3.5.4. The other note worth observation is that the density of bubbles increases as the rate of helium implantation increases.

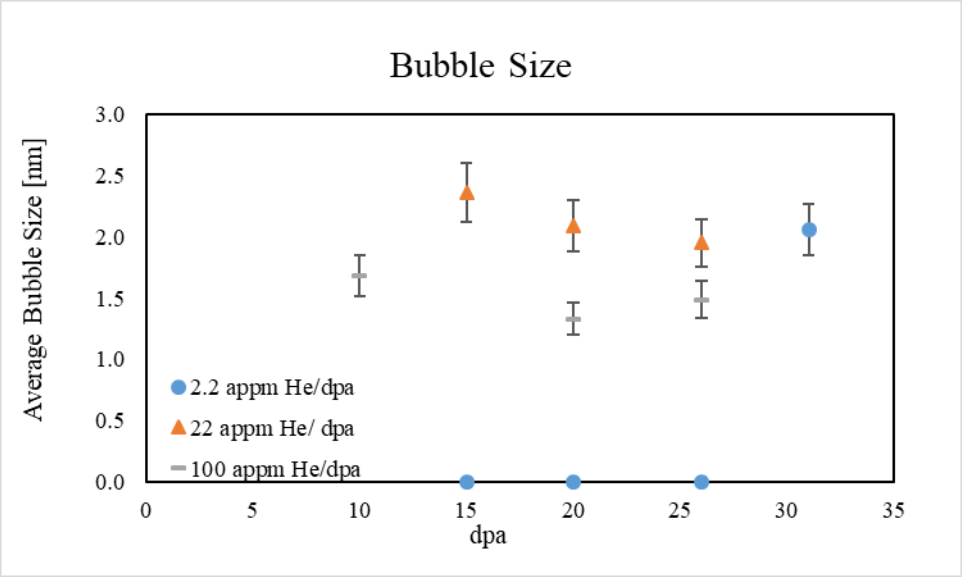

Figure 3.5.4: Average bubble size for the dual-beam irradiation of HT9 for implantation rates of 2.2, 22 and 100 appm He/ dpa.

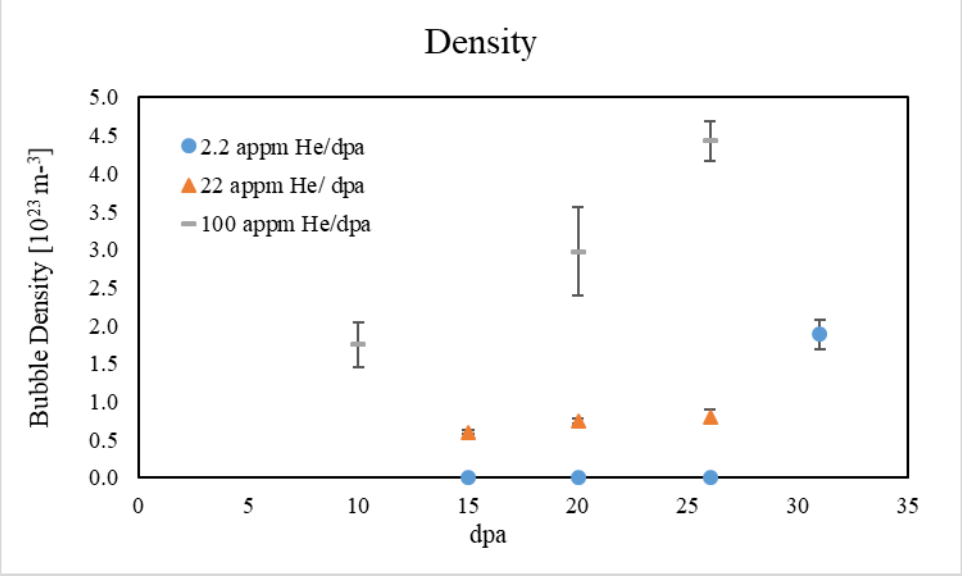

Figure 3.5.5: Average bubble density for the dual-beam irradiation of HT9 for implantation rates of 2.2, 22 and 100 appm He/ dpa.

Table 3.5.2 below shows the average of the five largest bubbles in each case. What can be overserved on this table is the change of the largest bubble with changes in dose and helium implantation.

Table 3.5.2: Max bubble size values.

Name	Max Bubble Size [nm]
15 dpa 33 appm He	No Observation
20 dpa 44 appm He	No Observation
26 dpa 57.2 appm He	No Observation
31 dpa 68.2 appm He	2.4±0.2
15 dpa 330 appm He	3.4±0.3
20 dpa 440 appm He	3.3±0.3
26 dpa 572 appm He	3±0.3
10 dpa 1000 appm He	2.6±0.3
20 dpa 2000 appm He	2±0.2
26 dpa 2600 appm He	2.2±0.2
0 dpa 221 appm He	No Observation
0 dpa 331 appm He	2.5±0.3
10 dpa 331 appm He	3±0.3
15 dpa 331 appm He	1.7±0.2

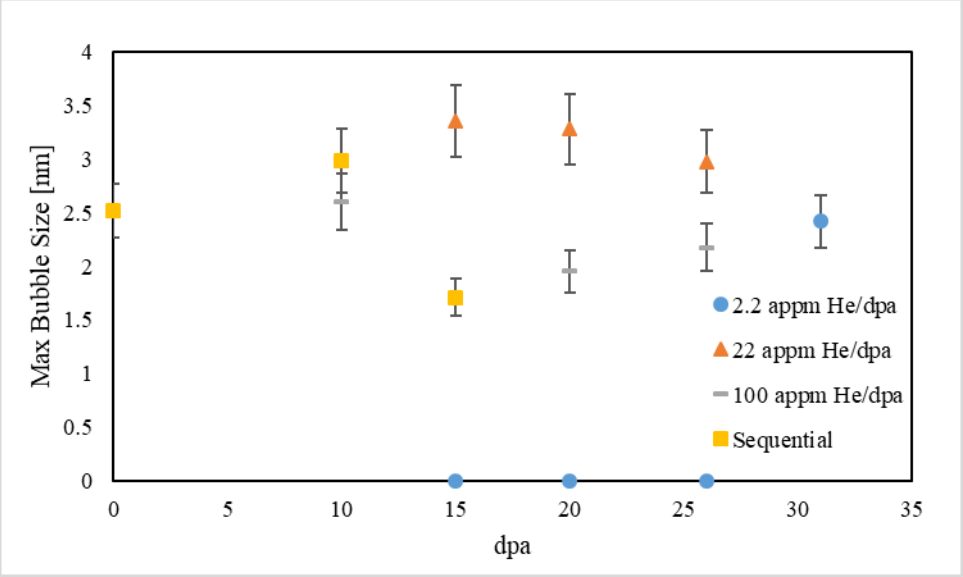

Figure 3.5.6: Max bubble size for irradiation case where the average of the 5 largest bubbles was taken for the size.

What can be seen on this table is that for the 22 appm He per dpa case the largest bubble continues to decrease in size. In the case of 1000 appm He per dpa it also decreases from 10 dpa but then appears to begin to grow in size again. For the sequential pre-implantation of helium, the bubbles first grow in size but then are reduced. What can be observed in figure 3.5.6 is that the dual-beam has a similar behavior to the average size where the 22 appm He/dpa is largest and as the rate is increased, the size is decreased. A noteworthy observation comes from the sequential data; the size increases when appm helium is increased with no damage and initially increases when then the damage is induced but then decreases with increased damage.

CHAPTER 4:

DISCUSSION

4.1 Effect of sequential irradiation vs. dual-beam on bubble size and density

The results show that during sequential irradiation where HT9 is implanted with 331 appm helium, followed by gold ion irradiation to 15 dpa, the He bubbles are smaller but more numerous than in the “equivalent” case of the dual-beam (15 dpa with 330 appm helium. The nucleation rate is larger for the sequential helium implantation than for the dual-beam but the bubbles grow more under dual-beam. Also, as seen in the bubble size distribution shown in figure 3.1.4 for sequential irradiation, it has a smaller spread of sizes compared to the dual-beam (figure 3.2.3, 3.3.3 and 3.4.3). The same trend was observed in a study conducted by Packan and Farrell [35] at 900 K (627ºC) in Alloy P7 (Fe-17Cr-16.7Ni-2.5Mo) (a similar material to 316 SS) where the cavity diameter increased in the order of (i) pre-implantation at room temperature (RT), (ii) pre-implantation at 900K, (iii) single beam irradiation, (iv) dual-beam irradiation, and finally (v) triple beam irradiation. The beams used were 4.0 MeV Ni ions, helium at a rate of 20 He appm/dpa and deuterium at a rate of 50 D appm/dpa to doses of 1, 10 and 70 dpa. As for the bubble density in Packan and Farrell [35] study, both pre-implanted cases resulted in a higher number density of bubbles than the single beam, dual beam and triple beam cases. Both these trends held for 1 to 70 dpa in their study. The ”nucleant” role of helium in dual-beam irradiation seems less efficient than in sequential irradiation as the concomitant point defect formation may help the implanted He to migrate more easily. In terms of growth, bubbles during dual-beam irradiation are larger which is explained by Packan and Farrell who proposed that implanted helium ions are continuously absorbed, by pre-existing cavities instead of creating new nucleation sites [35]. It would be expected to have a larger density but smaller bubble size in the

room temperature implanted case since helium that is implanted at room temperature can migrate in di-vacancies through substitutional mechanism [36]. When the temperature is elevated during implantation the diffusivity would be enhanced, this would allow for more interaction of the existing vacancy-helium pairs to grow into larger bubbles while also reducing their number which is seen by Packan and Farrell study [35].

There have also been experiments done on 304 SS comparing dual-beam and pre-implanted cases of 200 appm helium. More precisely, three study cases were investigated (i) pre-implantation at 25 °C, (ii) pre-implantation at temperature (650, 700 and 750 °C), and (iii) dual-beam irradiation (at 80 He appm/dpa) with 28 MeV Si^{6+} to a dose of ~40 dpa [37, 38]. They observed that dual-beam irradiation led to an average bubble size smaller than for the pre-implantation at temperature but larger than for the case of pre-implantation at room temperature, indicating an effect of the pre-implantation temperature [37]. The bubble densities had the opposite trends. This is in contrast to our study and with the previously mentioned study [35]. It has been suggested that this difference between 304 and other austenitic alloys may be due to the radiation-induced phase decomposition that 304 SS can undergo and to the fact that cavities and acicular precipitates have coupled growth [39]. HT9 and the stable austenitic alloy [35] have the same trends which suggest they have the same underlining mechanism which was helium is a “nucleant” during preimplantation and during dual-beam irradiation it is continuously absorbed at the existing cavities. Some other differences between 304 and HT9 also could play a role. There are more grain boundaries in ferritic/martensitic HT9, due to the lath structure than in 304 SS, which could explain why it is harder for bubbles to nucleate as grain boundaries are defect sinks and absorb both vacancies and interstitials [40]. This means there are fewer places for the gas atoms to interact with vacancies to form new bubbles or cause the growth of existing

bubbles. This seems to play a minor part compared to the radiation-induced phase decomposition that 304 undergoes.

Thus, regardless of the structure (austenitic (304SS, and P7) or F/M), a difference between sequential irradiation and dual beam irradiation in terms of the resulting He bubble size and number density for equivalent He implantation and dpa level. This difference between pre-implantation versus dual implantation can be due to the continuous absorption of helium by pre-existing cavities in dual-beam irradiation or it could result from the super-saturation of vacancies before irradiation damage [35, 41]. In our case, since the level of vacancy concentration due to the He implantation is rather negligible (especially compared with the vacancies induced by the heavy ions), it is more likely that the difference arises from the former hypothesis that helium is continuously absorbed by pre-existing bubbles during the dual-beam irradiations. In the literature other sequential studies have been done, Kai and Kulcinski [23] where HT9 was pre-implanted with 100 appm He then irradiated with 14 MeV Ni ions at 400°C to 600°C with doses of 10, 30 and 60 dpa. Helium bubbles were only observed at 500 °C at 30 dpa but not 10 or 60 dpa, and at 600°C at 10 and 30 dpa, 60 dpa was not reported for 600°C [23].

The temperature effect suggested by [37] needs further investigation especially since the trends observed are somewhat in contrast with the study on P7 (also austenitic) [35] and our study on HT9 (F/M).

4.2 Effect of helium appm/dpa rate on the He bubble size and number density during dual-beam irradiations

4.2.1 Comparison to neutron-irradiated HT9

Firstly, it should be mentioned that the actual helium/dpa ratios used in this study based on a neutron irradiation condition investigated in the same alloy heat in the BOR 60 reactor for

which the helium appm/dpa ratio was 0.22 [1, 19]. This value was not achievable in the in-situ experimental set-up at JANNuS so values of 2.2 (one order of magnitude larger) and 22 (two orders of magnitude higher) were chosen, as well as the higher value of 100 which was added for comparison. In Zheng et al. [1, 19] on neutron-irradiated HT9 unimodal size distributions were reported at temperatures of 377 °C at 17.1 dpa and 457°C at 14.6 dpa and bimodal distributions were observed at 377 °C at 35.1 dpa and 417 °C at 18.6 dpa. In this study, all the measurements showed a unimodal size distribution. The cavity sizes for smaller than 2 nm ranged from 1.1 for 377°C to 1.5 for 457°C, while dual-beam irradiation at 100 helium appm/dpa had bubble sizes from 1.3 to 1.7 for 20 and 10 dpa respectively. This shows that the bubble size is similar to the neutron counterpart. A difference between the studies is that dual-beam irradiation with any helium/dpa ratio at any dose did not produce a bimodal distribution while neutron-irradiation does as seen in [1, 19]. There is a variance in the densities, at 100 he appm/dpa for 10 and 20 dpa is 1.8 and $3.0*10^{23}$ m^{-3} which is similar to the 377°C at 17.1 dpa density of $2.5*10^{23}$ m^{-3}, a difference here is that as dual beams dose increased the density increased but for the neutron-irradiated case at 35.1 dpa the density had decrease [1, 19]. For neutron-irradiation at 417°C, 22 helium appm/dpa has the closest density values but they do not mimic the bimodal size distribution [1, 19]. For 457°C the sequential case had the same density at 15 dpa with 331 appm helium preinjected. This shows that dual-beam is a viable method to emulate neutron damage and the effects of nuclear reactions.

4.2.2 Comparison to experiments in HT9 in the literature

As seen in figures 3.5.4 and figure 3.5.5 the rate of implanting helium has an effect. The larger the helium implantation rate per dpa the smaller the helium bubble will be but inversely the larger the density of bubbles will be. The trend observed in our study is very similar to the

trend observed by Monterrosa et al. who carried out dual-beam irradiations on bulk HT9 at 460 °C with 5 MeV Fe^{2+} ions with helium appm/dpa from 0 to 0.2 with dpa values up to 188 dpa, followed by ex-situ characterization [42]; it is worth mentioning that in their study, they considered the influence of beam-induced carbon uptake as well. In both their study and this study, the bubble size decreased and density increased as the He appm/dpa ratio increased in the specific ranges of appm/dpa ratio values investigated in the two studies respectively. This shows that helium in-situ TEM irradiation results led to similar trends as the bulk irradiation. What can also be seen in their study is that at 0.2 He appm/dpa the effect of carbon uptake can't be distinguished from the shielded case. This would suggest that in this study which has high rates, the carbon intake in the TEM column, if any, may have a negligible effect. Also, in a review by Odette et al. [43] that covers the effects of charged-particles and helium implantation on the microstructure of stainless steels and neutron-irradiated 316 in two different reactors, EBR-II and HFIR. By increasing the helium appm/dpa ratio is reported to result in larger bubble density and smaller bubbles which is in agreement with this study.

In another study [21] on bulk HT9 irradiated with dual-beam (at 15 He appm /dpa) using 3 MeV Ni+ with a temperature range from 273-600 °. At 410 °C intergranular cavities, less than 5 nm were observed with a unimodal distribution, whereas at 470 °C a bimodal size distribution [21]. At 530°C and 600°C they observed small cavities less than 4 nm that were most prevalent on martensitic lath boundary or intergranular dislocations [21]. In a study by Asano et al. [22], HT9 underwent bulk dual-beam irradiation using 3.0 MeV Ni^{+} and 0.83 MeV He^{+} ions with a ratio of 15 He appm/dpa with a temperature range from 350°C to 600°C to 25 dpa. They observed small uniform cavities that were less than 4 nm in size at 410°C [22]. At 470°C they observed bimodal size distribution and at 530°C and 600°C they cavities less than 5 nm at the

dislocations and lath boundaries [22]. This is similar to what is observed in this study done in situ in the TEM at 430°C where the bubbles are all less than 5 nm and have a unimodal size distribution and the temperatures are similar. None of the bubbles were able to reach the critical radius or the critical number of helium atoms within the bubble to allow for larger bubbles to grow to form the bimodal distribution. In the study by Asano et al. [22] they reported a critical radius of around 3 nm for the temperature of this study, 430°C. Their study has a different helium appm/dpa ratio, this study had a case above and below it and neither reached a critical radius we can assume the critical radius will be a similar size. In Yamamoto et al. [44] study on tempered martensitic steel with 8 wt.% Cr with dual-beam irradiation (47 and 48 He appm/dpa) to 26 and 10 dpa using 6.4 MeV Fe^{3+} and 1 MeV He^{2+} ions and 1210 and 480 He appm at 500 ºC, they used a threshold of 4 nm. It seems that a critical radius of about 3-4 nm seems to be the consensus for such studies, which is also in contrast with the value from the BOR 60 experiments [1, 19] when they found a critical radius of 2 nm to form a bimodal distribution. It can be concluded that while some bubbles were near the threshold they had yet to reach the required number of helium atoms the change the growth mechanism or that the dose was not high enough.

4.2.3 Comparison to other Steels

In the study by Yamamoto et al. [44] in tempered martensitic steel (Fe-8Cr) They observed bubbles from 1 nm to 20 nm voids. The small helium bubbles are observed in this study but the large voids are not. There can be several reasons for this difference one being temperature, diffusion is enhanced which could help with bias-growth mechanism, and the dose was also much larger than observed in this study. Another reason would be the temperature, 500 °C has been shown to be the peak swelling temperature of HT9 by Smidt et al. [45].

There have been studies on the effect of He appm/dpa on AISI 316 by Katoh et al. [46] to create a theoretical model to describe the microstructural changes. In their study they compared different He appm/dpa rates up to 25 dpa at a temperature of 873 K, using 4 MeV Ni^{3+} and 1 MeV He^{2+} ions in bulk samples. They also reported that the higher the appm/dpa rates the larger the bubble density [46]. This is consistent with our observations on the densities; the bubble density response to dose increases with the helium appm/dpa and the amount of helium within the samples. In addition, for the same helium appm/dpa, an increasing dose would increase the bubble density, which is also observed in our study. There is also a linear relationship between the bubble densities at the same dose as a function of helium appm/dpa. This is also an observed trend in this study.

4.2.4 Bubble-to-void conversion

Katoh et al. [47] reported that the He appm/dpa ratio does have an effect on the bubble-to-void conversion. In low He appm/dpa ratios (4-15 helium appm/dpa), it occurred faster than for higher ratios (50 helium appm/dpa). This was supported by the results by Monterrosa et al. [42]. What is changing in the microstructure is the required critical radius for the bias growth model. In the case of higher helium appm/dpa, the vacancy clusters' growth is hindered due to reduced net vacancy flux [47]. What is defined as a bubble would be a bubble that has not reached the critical radius to shift to bias growth; once it reaches that radius it is called a void in their study. It was suggested by Stoller [48] that high cavity sink strength causes an increase in the recombination of point defects at the cavity, which in turn reduces the saturation of point defects and hinders bubble-to-void conversion by increasing the critical number of gas atoms for void formation. This can be exacerbated by a second method of delaying the bubble-to-void conversion which is by diluting the helium and vacancies to a large number of cavities to lower

the rate at which bubbles reach the critical size. A method to cause this is fine precipitates as bubbles will form there [49]. When helium is co-implanted with ion irradiation damage the interstitial atoms created by ion damage compete with helium to interact with the vacancies [50]. If the interstitials are faster, the vacancies are annihilated but if the helium can interact, several things can occur. The helium atom can be trapped in the vacancy, high order vacancies, can form a helium-vacancy complex, the helium can also migrate as an interstitial atom or di-vacancy [50].

In a study done on a (Fe-16.22Ni-14.57Cr-2.37Mo-1.79Mn) alloy by Sekimura et al. [51], which is basically a titanium modified stainless steel 316 alloy. Sekimura et al. [51] studied the effects of two different dual-beam implantation rates (15 and 75 He appm/dpa) and compared it to pre-implantation of 20 appm He and irradiation by a 0.4 MeV Al^{+} ions to 50 dpa. They observed that the larger the He appm/dpa ratio, the larger the density over the various temperature ranges from 427 to 650 °C. The bubble size in their study between 427 and 527°C was very similar for both dual-beam conditions along with the pre-implanted and single beam irradiation [51]. In their study the bubble size varies, for low temperatures, they are very similar and with elevated temperatures the 75 appm He/dpa is larger than 15 appm He/dpa. This is different from what literature says and this study observes. This could be caused by the composition of modified 316 austenitic steel, where the titanium is usually expected to form a large density of small carbides.

The overarching trend for bubble density is that as the He appm/dpa increases so does the density of the bubbles. Moreover, the larger the He appm/dpa the more responsive the bubble density becomes to dpa. Based on our observations, two observations can be made: (i) as the dose and helium concentration increases the density of cavities increases; and (ii) as the He

appm/dpa increases the bubble size gets smaller; indeed, at the low He appm/dpa ratio, bubbles did not become visible until doses greater than 26 dpa with 57.2 appm He whereas, for the larger appm/dpa ratio, there is sufficient helium to stabilize the vacancies and grow into visible bubbles with a lower dose. These two trends are supported by other studies of dual-beam experiments [42, 43, 47]:

4.3 Effect of sequential irradiation order

4.3.1 Irradiation then implantation versus dual-beam irradiation

In a study on 316L [8, 9], Jublot-Leclerc et al. compared (i) dual-beam irradiation using 4 MeV Au^{2+} and 10 keV He^{+} ions, (ii) single-ion irradiation (without He), and heavy-ion irradiation followed by helium implantation at 450°C and 550°C. They reported that the dual-beam (250 appm/dpa) and single irradiation (only Au^{2+} irradiation) led to cavities with similar sizes at 450°C. In their case study with post helium implantation at 550 °C, the helium does not cause more nucleation but grows the existing cavities and helps with the coalescence of cavities. The cavities grow by the direct absorption of helium atoms injected into the matrix [8].

4.3.2 Implantation then irradiation versus dual-beam irradiation

In the study on alloy P7 already mentioned earlier it was shown that dual-beam irradiation produced larger bubbles then pre-implantation of both at RT or irradiation temperature followed by irradiation but had a lower number density [35]. In the study by Farrell and Packan [41] on the same alloy when they were testing the effect of temperature it was shown that single ion-beam (no helium) had a smaller density of cavities compared to dual-beam and triple-beam (helium + hydrogen + nickel ion) irradiation for all temperatures at 1 and 70 dpa when it had cavities. At 1 dpa, the observed trend was single nickel irradiation resulted in larger

cavities than dual-beam but the size decreased at 1025 K and became smaller then dual-beam as there are no visible cavities.

4.3.3 The role of Helium

The role of helium in the sequential irradiation i.e implantation then irradiation is to act as a nucleant. When helium is inserted during dual-beam irradiation it can both nucleate new cavities and be absorbed by the pre-existing ones to promote growth. In the case found in the literature where irradiation was followed by implantation, helium was only absorbed by the existing cavities but did not nucleate any new cavities.

4.3.4 Role of Heavy-ion irradiation after helium implantation

In the sequential implantation case first the HT9 sample was implanted with 10 keV helium ions to a concentration of 331 appm He. At this point bubbles were already present before the sample was irradiated with Au ions. Interestingly the average bubble size did not change after the heavy ion irradiation as can be seen in figure 3.1.3, however, when looking at the size distribution (shown in figure 3.1.4), it became broader and slightly shifted to the right. Also, there was a clear increase in the density of bubbles as seen in figure 3.1.5. There are two methods for the density to increase. The first would be to split the existing bubbles with the irradiation damage. Even if such a mechanism was possible, this would be rather unlikely since the size distribution shifted to the right not left. If the larger bubbles were being split, even larger bubbles would not form, which was in fact observed. The other scenario would be that the point defects (essentially the vacancies produced by the ion irradiation) enhance the mobility of the helium that was trapped in solution or in clusters (that were not TEM visible prior to the heavy-ion irradiation) [50]. This would allow for the creation of new bubbles and to grow the existing ones and it could also explain the broadening of the size distribution.

In the literature, sequential irradiation (i.e. implantation then irradiation) was also done on T91 with various levels of implanted He (0, 1, 10, 100, or 1000 appm) into the sample using 400 keV He ions at room temperature. Then the samples were irradiated to dpa levels ranging from 45 to 356 dpa at 460°C [52]. They observed that as the helium concentration increased for the same dose level the bubble size would decrease but their density would increase.

CHAPTER 5:

CONCLUSIONS

In this study, the formation of He bubbles in HT9 alloy was investigated through the use of in-situ Transmission Electron Microscopy coupled with He implantation and Heavy ion irradiation. Of particular interest was the effect of increasing the He appm/dpa ratio on the formation and growth of the bubbles, as well as the effect of the sequential order of irradiation i.e. He-pre-implantation followed by Heavy ion irradiation versus true dual-beam irradiation. In such experiments, helium is implanted to emulate the (n, α) reactions that occur in a nuclear reactor.

During the in-situ dual-beam irradiations, three different Helium appm/dpa rates were probed: 2.2, 22 and 100, respectively. It was observed that the larger the rate of helium/dpa the larger the bubble density and the smaller the size of the bubbles. The bubble density showed a linear increase with dose (dpa) and He concentration (appm) for the ranges investigated. Also it is worth mentioning that the “threshold” dose at which visible bubbles can be imaged with TEM decreases with increasing He appm/dpa ratio.

During the sequential irradiation where helium implantation was followed by heavy ion irradiation, the role of helium as a “nucleant” was evident where visible bubbles were imaged at 331 He appm before the heavy ion irradiation started; the subsequent heavy ion irradiation did not increase the size of bubbles, however, it increased their density. This is to be put in contrast with the dual-beam case where visible bubbles were imaged at lower accumulated He appm concentration with the help of the vacancies produced by the concomitant heavy ion irradiation. The dual-beam irradiation seemed to lead to a smaller density of bubbles but of larger sizes for a given dose (in dpa).

REFERENCES

1. Zheng, C., et al., Microstructure response of ferritic/martensitic steel HT9 after neutron irradiation: effect of dose. Journal of Nuclear Materials, 2019. **523**: p. 421-433.

2. Kai, J.J. and G.L. Kulcinski, The effects of heat treatment on the microstructural evolution of HT-9 ferritic steel. Scripta Metallurgica, 1989. **23**(7): p. 1151-1156.

3. D. Kaoumi, C.Z., E. R. Reese, K. G. Field, E. Marquis. Microstructure Characterization of neutron irradiated Ferritic/Martensitic steel HT9. in Symposium on Qualification, Development and Modeling of Structural and Fuel Materials for Sustainable Nuclear Reactors. 2019. Stockhlom, Sweden: EUROMAT 2019.

4. Zheng, C., et al., Radiation induced segregation and precipitation behavior in self-ion irradiated Ferritic/Martensitic HT9 steel. Journal of Nuclear Materials, 2017. **491**: p. 162-176.

5. Garner, F.A., M.B. Toloczko, and B.H. Sencer, Comparison of swelling and irradiation creep behavior of fcc-austenitic and bcc-ferritic/martensitic alloys at high neutron exposure. Journal of Nuclear Materials, 2000. **276**(1): p. 123-142.

6. Klueh, R.L. and A.T. Nelson, Ferritic/martensitic steels for next-generation reactors. Journal of Nuclear Materials, 2007. **371**(1): p. 37-52.

7. Zinkle, S.J. and G.S. Was, Materials challenges in nuclear energy. Acta Materialia, 2013. **61**(3): p. 735-758.

8. Jublot-Leclerc, S., et al., Cavity nucleation and growth in dual beam irradiated 316L industrial austenitic stainless steel. Journal of Nuclear Materials, 2017. **494**: p. 240-251.

9. Jublot-Leclerc, S., et al., TEM study of the nucleation of bubbles induced by He implantation in 316L industrial austenitic stainless steel. Journal of Nuclear Materials, 2015. **466**: p. 646-652.

10. Ziegler, J.F., M.D. Ziegler, and J.P. Biersack, SRIM – The stopping and range of ions in matter (2010). Nuclear Instruments and Methods in Physics Research Section B: Beam Interactions with Materials and Atoms, 2010. **268**(11): p. 1818-1823.

11. Norgett, M.J., M.T. Robinson, and I.M. Torrens, A proposed method of calculating displacement dose rates. Nuclear Engineering and Design, 1975. **33**(1): p. 50-54.

12. Kinchin, G.H. and R.S. Pease, The Displacement of Atoms in Solids by Radiation. Reports on Progress in Physics, 1955. **18**(1): p. 1-51.

13. Standard Practice for Neutron Radiation Damage Simulation by Charged-particle Irradaiation. E521-96, Annual Book of ASTM Standards, 2004. **12.02**.

14. Juslin, N., et al., Simulation of threshold displacement energies in FeCr. Nuclear Instruments and Methods in Physics Research Section B: Beam Interactions with Materials and Atoms, 2007. **255**(1): p. 75-77.

15. Shao, L., et al., Effect of defect imbalance on void swelling distributions produced in pure iron irradiated with 3.5MeV self-ions. Journal of Nuclear Materials, 2014. **453**(1): p. 176-181.

16. Gelles, D.S., Development of martensitic steels for high neutron damage applications. Journal of Nuclear Materials, 1996. **239**: p. 99-106.

17. Murty, K.L. and I. Charit, Structural materials for Gen-IV nuclear reactors: Challenges and opportunities. Journal of Nuclear Materials, 2008. **383**(1): p. 189-195.

18. Frazer, D., et al., Degradation of HT9 under simultaneous ion beam irradiation and liquid metal corrosion. Journal of Nuclear Materials, 2016. **479**: p. 382-389.

19. Zheng, C., et al., Microstructure response of ferritic/martensitic steel HT9 after neutron irradiation: Effect of temperature. Journal of Nuclear Materials, 2020. **528**: p. 151845.
20. Ke, J.-H., et al., Cluster dynamics modeling of Mn-Ni-Si precipitates in ferritic-martensitic steel under irradiation. Journal of Nuclear Materials, 2018. **498**: p. 83-88.
21. Suzuki, K., et al., Cavity growth in dual-ion and electron irradiated HT-9 ferritic stainless steels. Journal of Nuclear Materials, 1985. **133-134**: p. 632-635.
22. Asano, K., et al., Microstructural evolution of HT9 under dual-beam charged particle irradiation. Journal of Nuclear Materials, 1988. **155-157**: p. 912-915.
23. Kai, J.J. and G.L. Kulcinski, 14 MeV nickel-ion irradiated HT-9 ferritic steel with and without helium pre-implantation. Journal of Nuclear Materials, 1990. **175**(3): p. 227-236.
24. Getto, E., et al., Effect of pre-implanted helium on void swelling evolution in self-ion irradiated HT9. Journal of Nuclear Materials, 2015. **462**: p. 458-469.
25. Getto, E., et al., Effect of irradiation mode on the microstructure of self-ion irradiated ferritic-martensitic alloys. Journal of Nuclear Materials, 2015. **465**: p. 116-126.
26. Pareige, C., V. Kuksenko, and P. Pareige, Behaviour of P, Si, Ni impurities and Cr in self ion irradiated Fe–Cr alloys – Comparison to neutron irradiation. Journal of Nuclear Materials, 2015. **456**: p. 471-476.
27. Zheng, C., et al., Correlation of in-situ transmission electron microscopy and microchemistry analysis of radiation-induced precipitation and segregation in ion irradiated advanced ferritic/martensitic steels. Scripta Materialia, 2019. **162**: p. 460-464.
28. Kaoumi, D. and C. Zheng, Microstructure Characterization of Ion-irradiated Ferritic/Martensitic HT9 Steel. Microscopy and Microanalysis, 2017. **23**(S1): p. 2214-2215.
29. Zheng, C. and D. Kaoumi, Radiation-induced swelling and radiation-induced segregation & precipitation in dual beam irradiated Ferritic/Martensitic HT9 steel. Materials Characterization, 2017. **134**: p. 152-162.
30. Wang, X., et al., Void swelling in ferritic-martensitic steels under high dose ion irradiation: Exploring possible contributions to swelling resistance. Scripta Materialia, 2016. **112**: p. 9-14.
31. Schneider, C.A., W.S. Rasband, and K.W. Eliceiri, NIH Image to ImageJ: 25 years of image analysis. Nat Methods, 2012. **9**(7): p. 671-5.
32. JANNuS (Joint Accelerators for Nano-science and Nuclear Simulation) Http://jannus.in2p3.fr and Http:/www.csnsm.in2p3.fr/MET.
33. Gentils, A. and C. Cabet, Investigating radiation damage in nuclear energy materials using JANNuS multiple ion beams. Nuclear Instruments and Methods in Physics Research Section B: Beam Interactions with Materials and Atoms, 2019. **447**: p. 107-112.
34. M L Jenkins, M.A.K., Characterization of Radiation Damage by Transmission Electron Microscopy, in Characterization of Radiation Damage by Transmission Electron Microscopy. 2001, Institute of Physics Publishing: **Bristol and Philadelphia**.
35. Packan, N.H. and K. Farrell, Simulation of first wall damage: Effects of the method of gas implantation. Journal of Nuclear Materials, 1979. **85-86**: p. 677-681.
36. Reed, D., A review of recent theoretical developments in the understanding of the migration of helium in metals and its interaction with lattice defects. Radiation Effects, 1977. **31**(3): p. 129-147.
37. Choyke, W.J., et al., Helium effects in ion-bombarded 304 stainless steel. Journal of Nuclear Materials, 1979. **85-86**: p. 647-651.

38. McGruer, J.N., et al., The effects of sequential and simultaneous helium implantation on void formation in a 304 stainless steel. Journal of Nuclear Materials, 1978. **74**(1): p. 174-177.
39. Farrell, K., Experimental effects of helium on cavity formation during irradiation—a review. Radiation Effects, 1980. **53**(3-4): p. 175-194.
40. Was, G.S., Fundamentals of radiation materials science : metals and alloys. 2007, Berlin: Berlin : Springer, 2007.
41. Farrell, K. and N.H. Packan, A helium-induced shift in the temperature dependence of swelling. Journal of Nuclear Materials, 1979. **85-86**: p. 683-687.
42. Monterrosa, A.M., et al., The influence of carbon on cavity evolution in ion-irradiated ferritic-martensitic steels. Journal of Nuclear Materials, 2018. **509**: p. 722-735.
43. Odette, G.R., P.J. Maziasz, and J.A. Spitznagel, Fission-fusion correlations for swelling and microstructure in stainless steels: Effect of the helium to displacement per atom ratio. Journal of Nuclear Materials, 1981. **104**: p. 1289-1303.
44. Yamamoto, T., et al., A dual ion irradiation study of helium–dpa interactions on cavity evolution in tempered martensitic steels and nanostructured ferritic alloys. Journal of Nuclear Materials, 2014. **449**(1): p. 190-199.
45. F. A. Smidt, P.R.M.J.A.S.J.E.W., Swelling Behavior of Commercial Ferritic Alloys, EM-12 and HT-9, as Assessed by Heavy Ion Bombardment
Irradiation Effects on The Microstructure and Properties of Metals. 1976, West Conshohocken, PA: ASTM International. 227-241.
46. Katoh, Y., et al., The influence of He/dpa ratio and displacement rate on microstructural evolution: a comparison of theory and experiment. Journal of Nuclear Materials, 1994. **210**(3): p. 290-302.
47. Katoh, Y., Y. Kohno, and A. Kohyama, Dual-ion irradiation effects on microstructure of austenitic alloys. Journal of Nuclear Materials, 1993. **205**: p. 354-360.
48. Stoller, R.E., The influence of helium on microstructural evolution: Implications for DT fusion reactors. Journal of Nuclear Materials, 1990. **174**(2): p. 289-310.
49. Mansur, L.K., et al., Control of helium effects in irradiated materials based on theory and experiment. Journal of Nuclear Materials, 1986. **141-143**: p. 633-646.
50. Ghoniem, N., et al., Theory of helium transport and clustering in materials under irradiation. Journal of Nuclear Materials, 1983. **117**: p. 96-105.
51. Sekimura, N., et al., The effect of helium on the microstructural evolution in PCA as studied by dual beam irradiation. Journal of Nuclear Materials, 1984. **122**(1): p. 322-326.
52. Monterrosa, A.M., Z. Jiao, and G.S. Was, The influence of helium on cavity evolution in ion-irradiated T91. Journal of Nuclear Materials, 2018. **509**: p. 707-721.